# Downloaded from https://www.science.org at Tsinghua University on October 12, 2025

#### RESEARCH ARTICLE SUMMARY

#### **IMMUNOLOGY**

# T cell cholesterol transport links intestinal immune responses to dietary lipid absorption

Yajing Gaot, John P. Kennellyt, Xu Xiao, Emily Whang, Alessandra Ferrari, Alexander H. Bedard, Julia J. Mack, Alexander Nguyen, Sonal Srikanth, Thomas Weston, Lauren F. Uchiyama, Whitaker Cohn, Danielle H. Cho, Min Sub Lee, Julian Whitelegge, Yousang Gwack, Stephen G. Young, Steven J. Bensinger, Peter Tontonoz\*



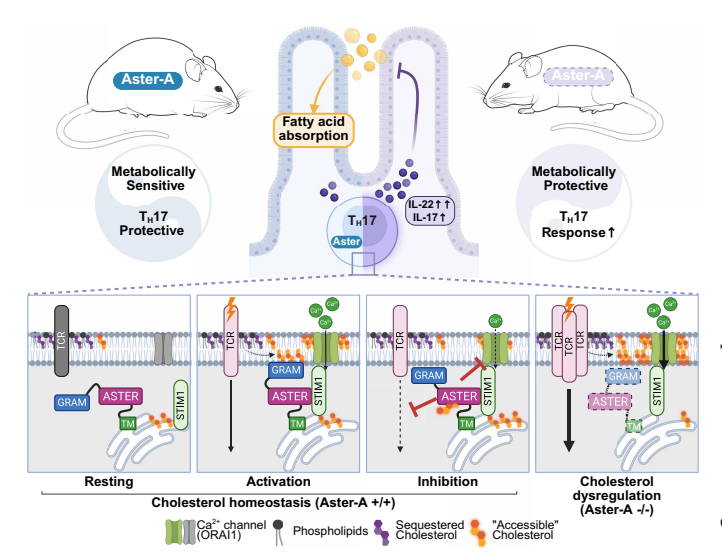
author affiliations: https://doi.org/10.1126/ science.adt4169

**INTRODUCTION:** Impaired lipid flux can lead to cellular and tissue dysfunction in human diseases, yet the pathways that maintain membrane lipid homeostasis remain incompletely defined. Immune cells, which must adapt to evolving threats and distinct microenvironments, may be especially reliant on their ability to reorganize membranes for optimal function. The initiation and resolution of immune responses also likely require timely recalibration of the cellular lipid repertoire. Whether and how immune cell membrane homeostasis affects organ function and systemic metabolism are incompletely understood.

RATIONALE: Cholesterol is an indispensable lipid component of the mammalian plasma membrane (PM). We previously characterized the Aster family of nonvesicular lipid transporters, which transfer cholesterol from the PM to the endoplasmic reticulum. Despite established links between cholesterol abundance and immune signaling, it is unknown how immune cells fine-tune membrane cholesterol.

**RESULTS:** We traced fatty acid uptake in the small intestine of mice and found that specific deletion of Aster-A in T cells reduced fatty acid absorption and conferred resistance to dietinduced obesity. Loss of Aster-A increased a gene expression signature associated with T helper 17 (T<sub>H</sub>17) cells among small intestine resident T cells. We found that Aster-A was highly expressed in T<sub>H</sub>17 cells and was indispensable for maintaining appropriate PM cholesterol levels in this cell type. Using specific cholesterol probes, we determined that T cell receptor (TCR) activation transiently increased the accessible PM cholesterol pool, which recruited Aster-A to restrain excess PM cholesterol accumulation. In the absence of Aster-A, excess PM cholesterol was funneled into a distinct cellular lipid pool, the sphingomyelinsequestered pool, leading to increased TCR nanoclustering. Consequently, Aster-A-deficient T<sub>H</sub>17 cells exhibited elevated TCR signaling and effector cytokine [interleukin-17 (IL-17) and IL-22] production. Proximity labeling in T cells revealed an interaction between Aster-A and stromal interaction molecule 1 (STIM1), a core component mediating Ca<sup>2+</sup> entry after TCR activation. We found that accessible PM cholesterol was required for TCR-induced Ca<sup>2+</sup> influx and that Aster-A dampened this process. Aster-A thus restrained both the early signals directly triggered by the TCR and the later signaling events that depend on Ca<sup>2+</sup> influx.

Single-cell transcriptomics and immune profiling further pinpointed increased IL-22 levels in T<sub>H</sub>17 cells from the small intestines of T cell-specific Aster-A-deficient mice. Acute administration of IL-22 before feeding was sufficient to suppress intestinal fatty acid uptake. Conversely, blocking IL-22 with neutralizing antibodies, genetic ablation of *Il22* from T cells, or antibiotic depletion of microbial signals that maintain gut T<sub>H</sub>17 cells each restored dietary fat absorption or diet-induced weight gain.



Nonvesicular cholesterol transport links intestinal T cell immunity to lipid absorption. T cell activation induces PM accumulation of accessible cholesterol and recruits Aster-A, which extracts cholesterol and transfers it to the endoplasmic reticulum to dampen TCR nanoclustering. Aster-A-STIM1 association at the PM further restrains Ca<sup>2+</sup> influx during TCR activation (indicated by a lightning bolt). Aster-A guards against excessive intestinal T<sub>H</sub>17 responses, thereby coordinating dietary lipid flux and systemic metabolism. GRAM, GRAM domain of Aster-A; ORAI1, calcium release-activated calcium modulator 1: TM, transmembrane domain of Aster-A. [Figure created with BioRender.com]

**CONCLUSION:** Our work identifies a rapid, on-demand regulator of immune membrane homeostasis. Aster-A responds to TCR activationinduced PM remodeling and subsequently removes excess membrane cholesterol to restrain TCR signaling cascades. We propose that membrane lipid remodeling may serve to promote microenvironmental adaptation by controlling tissue T cell reactivity. Dysregulation and accumulation of T cell PM cholesterol therefore has the potential to lead to aberrant gut T<sub>H</sub>17 effector function, alters immune-epithelial communication, and modulates intestinal and systemic nutrient metabolism.

Science 9 OCTOBER 2025 149

<sup>\*</sup>Corresponding author. Email: ptontonoz@mednet.ucla.edu †These authors contributed equally to this work. Cite this article as Y. Gao et al., Science 390, eadt4169 (2025). DOI: 10.1126/science.adt4169

#### **IMMUNOLOGY**

# T cell cholesterol transport links intestinal immune responses to dietary lipid absorption

Yajing Gao<sup>1,2</sup>†, John P. Kennelly<sup>1,2</sup>†, Xu Xiao<sup>1,2</sup>‡, Emily Whang<sup>1,2,3</sup>, Alessandra Ferrari<sup>1,2</sup>§, Alexander H. Bedard<sup>1,2</sup>, Julia J. Mack<sup>4,5</sup>, Alexander Nguyen<sup>1,2,6</sup>, Sonal Srikanth<sup>7</sup>, Thomas Weston<sup>8</sup>¶, Lauren F. Uchiyama<sup>1,2,5</sup>, Whitaker Cohn<sup>9</sup>, Danielle H. Cho<sup>1,2</sup>, Min Sub Lee<sup>10,11</sup>, Julian Whitelegge<sup>9</sup>, Yousang Gwack<sup>6</sup>, Stephen G. Young<sup>4,7</sup>, Steven J. Bensinger<sup>10,11</sup>, Peter Tontonoz<sup>1,2,5</sup>\*

The intrinsic pathways that control membrane organization in immune cells and their impact on cellular functions are poorly defined. We found that the nonvesicular cholesterol transporter Aster-A linked plasma membrane (PM) cholesterol availability in CD4 T cells to systemic metabolism. Aster-A was recruited to the PM during T cell receptor (TCR) activation, where it facilitated the removal of accessible cholesterol. Loss of Aster-A increased cholesterol accumulation in the PM, which enhanced TCR nanoclustering and signaling. Aster-A associated with stromal interaction molecule 1 (STIM1) and negatively regulated calcium (Ca<sup>2+</sup>) flux. Aster-A deficiency promoted CD4 T cells to acquire a T helper 17 (T<sub>H</sub>17) phenotype and stimulated interleukin-22 production, which reduced intestinal fat absorption and conferred resistance to diet-induced obesity. These findings delineate how immune cell membrane homeostasis links to systemic physiology.

The plasma membrane (PM) constitutes a major reservoir of unesterified cholesterol. The PM is thought to contain three cholesterol pools with distinct biochemical and biophysical properties (1): an essential pool required for membrane integrity and cell viability, a relatively inactive pool recognized by Ostreolysin A (OlyA) in which cholesterol is sequestered by sphingomyelin (SM) (2), and an active, or accessible, pool that can be readily mobilized and that can be detected by domain 4 of Anthrolysin O (ALOD4) (3, 4).

Cellular and external cues, such as the uptake of lipoprotein-derived cholesterol, activation of SM degradation, and infection, regulate the size of the accessible cholesterol pool (5–11). Excess PM accessible cholesterol can move to the endoplasmic reticulum (ER) for esterification or be effluxed to extracellular lipoprotein acceptors (6, 12–15). However,

<sup>1</sup>Department of Pathology and Laboratory Medicine, University of California, Los Angeles, Los Angeles, CA, USA. <sup>2</sup>Department of Biological Chemistry, University of California, Los Angeles, Los Angeles, CA, USA. <sup>3</sup>Department of Pediatrics, Division of Gastroenterology, Hepatology, and Nutrition, David Geffen School of Medicine, University of California, Los Angeles, Los Angeles, CA, USA. <sup>4</sup>Department of Medicine, Division of Cardiology, David Geffen School of Medicine, University of California, Los Angeles, Los Angeles, CA, USA. 5Molecular Biology Institute, University of California, Los Angeles, Los Angeles, CA, USA. <sup>6</sup>Vatche and Tamar Manoukian Division of Digestive Diseases, Department of Medicine David Geffen School of Medicine, University of California, Los Angeles, Los Angeles, CA, USA. <sup>7</sup>Department of Physiology, David Geffen School of Medicine, University of California, Los Angeles, Los Angeles, CA, USA. <sup>8</sup>Department of Human Genetics, David Geffen School of Medicine, University of California, Los Angeles, Los Angeles, CA, USA. <sup>9</sup>The Pasarow Mass Spectrometry Laboratory, University of California, Los Angeles, Los Angeles, CA, USA. 10 Department of Microbiology, Immunology and Molecular Genetics, University of California, Los Angeles, Los Angeles, CA, USA. 11 Department of Molecular and Medical Pharmacology, David Geffen School of Medicine, University of California, Los Angeles, Los Angeles, CA, USA. \*Corresponding author. Email: ptontonoz@mednet.ucla.edu †These authors contributed

equally to this work. ‡Present address: Saha Cardiovascular Research Center, Department of Physiology, University of Kentucky, Lexington, KY, USA. §Present address: Department of Nutritional Sciences and Toxicology, University of California, Berkeley, Berkeley, CA, USA. ¶Present address: Thermo Fisher Scientific, Hillsboro, OR, USA.

the functions of accessible cholesterol within the PM are poorly defined. The sole exception is hedgehog signaling in the primary cilium, where Patched-1 inactivation by Hedgehog ligands increases accessible cholesterol and potentiates the activation of Smoothened (8, 16).

Nonvesicular sterol transport is recognized as being important for maintaining appropriate lipid distribution between cellular membrane compartments (17, 18). The Aster proteins play an indispensable role in moving accessible cholesterol from the PM to the ER (5, 12, 19). Increased accessible PM cholesterol facilitates recruitment of the GRAM domain of Asters to the PM and the formation of PM-ER contact sites, through which the ASTER domain channels excess cholesterol to the ER (12, 19). Aster proteins are required for the efficient internalization, storage, and utilization of diet- and lipoprotein-derived cholesterol in various metabolic and steroidogenic organs (6, 12, 15, 20). Of particular interest, Aster-A is highly expressed in lymphoid organs (12), suggesting a yet-to-be-identified function for nonvesicular sterol transport in the immune system. How immune cell cholesterol homeostasis affects tissue-specific functions and systemic metabolism remains unexplored.

Studies involving chemical or indirect genetic approaches have reported that increasing PM cholesterol abundance can enhance T cell receptor (TCR) signaling (21–25). At the same time, cryo–electron microscopy (cryo-EM) structural studies have revealed that the resting  $\alpha\beta$ TCR core contains two free cholesterol molecules that may serve to maintain the inactive state (26, 27). Such studies imply that PM cholesterol availability must be tightly controlled during immune activation. However, it remains unknown whether T cells engage specific machinery to monitor and redistribute PM cholesterol. How membrane cholesterol dynamics are integrated with TCR signaling cascades has also not been defined.

#### Results

# Dietary fatty acid absorption is decreased in mice that lack Aster-A in T lymphocytes

We generated Aster-A-deficient mice to analyze potential contributions of this cholesterol transporter to systemic metabolism. We observed that whole-body deletion of Aster-A impaired fatty acid uptake by the small intestine (SI). We gavaged Aster-A-deficient  $(A^{-/-})$  or littermate control (A<sup>+/+</sup>) mice with [<sup>3</sup>H]triolein (18:1), a major fatty acid species in human and mouse diets, and measured the appearance of radioactivity in SI segments, plasma, and tissues (28, 29). A<sup>-/-</sup> mice showed lower <sup>3</sup>H counts in the jejunum and lower total SI <sup>3</sup>H levels after 2 hours (Fig. 1A and fig. S1A) and a delay in the plasma <sup>3</sup>H appearance compared with  $A^{+/+}$  controls (fig. S1B). In mice where Aster-A was deleted specifically in the liver, using Albumin  $^{Cre}$  ( $A^{\Delta Alb}$ ), or in the intestinal epithelium, using VillinCreERT ( $A^{\Delta Vil}$ ) (fig. S1C), the intestinal uptake of [3H]triolein was not altered (Fig. 1B-C), consistent with redundancy of Aster-A and -C in the liver and low Aster-A expression in SI epithelium (fig. S1D) (6, 15). Thus, the decreased fatty acid absorption in A<sup>-/-</sup> mice was not due to intrinsic effects on enterohepatic tissues.

We sought to identify cell types with prominent Aster-A expression. In public mRNA expression datasets from humans and mice, secondary lymphoid organs (spleen and lymph nodes) exhibited abundant transcripts for Aster-A (GRAMD1A/Gramd1a) and low levels of transcripts for Aster-B and -C (Gramd1b and Gramd1c) (fig. S1, E and F). Examination of immune cell types in the ImmGen database (30) revealed high and specific expression of Aster-A in conventional T cells (fig. S1G). In mice where Aster-A was depleted in T cells specifically using CD4<sup>Cre</sup> (referred to as  $A^{\Delta CD4}$  mice), Gramd1a transcripts in the CD4<sup>+</sup> and CD8<sup>+</sup> T cells were reduced by more than 100-fold and Aster-A protein levels were undetectable (fig. S2, A and B) compared with control mice that carried only floxed Gramd1a alleles (F/F).  $A^{\Delta CD4}$  mice were born at Mendelian frequencies and exhibited normal development, suggesting no gross signs of early-onset immune disorders (fig. S2, C and D).

Science 9 OCTOBER 2025 1 of 21

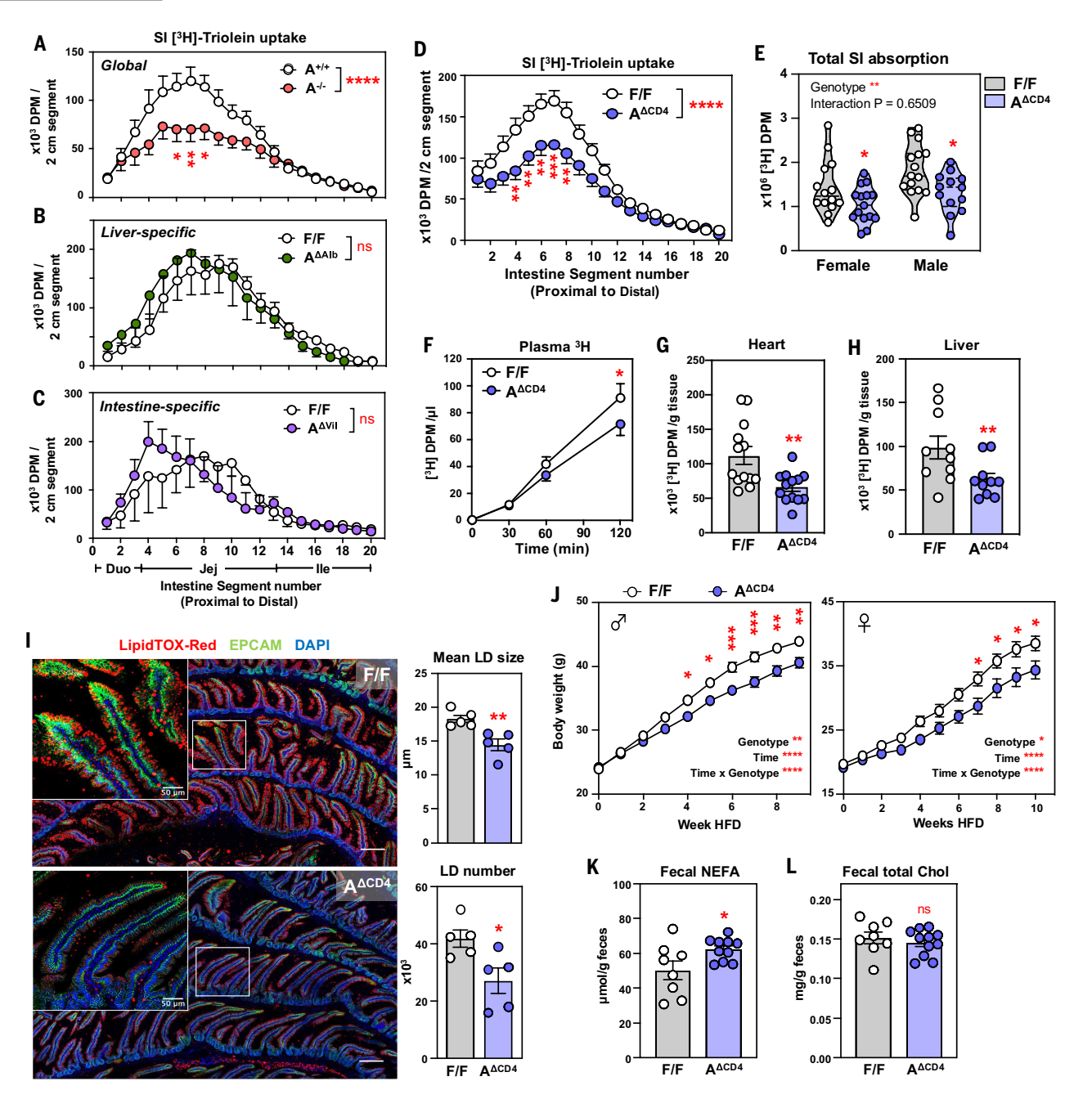


Fig. 1. Aster-A deficiency impairs fatty acid absorption in the SI and regulates diet-induced obesity. (A) Distribution of radioactivity in intestinal segments of Aster-A WT (A<sup>+/+</sup>, n = 13) and global deficient (A<sup>-/-</sup>, n = 14) littermate mice after an oral gavage of olive oil containing [<sup>3</sup>H]triolein (18:1) for 2 hours. DPM, disintegrations per minute. (B and C) Distribution of radioactivity in intestinal segments of liver (hepatocyte)-specific [A^Allb (B)] or intestinal epithelium–specific [A^VII (C)] Aster-A gene deletion (knockout) mice and their respective cre-negative floxed (F/F) littermate controls after an oral challenge of olive oil containing  $\lceil^3H\rceil$  triolein (18:1) for 2 hours (n=9 and 6 mice per group for liver-specific knockout mice; n = 4 mice per group for intestinal epithelium-specific mice). (D) Distribution of radioactivity in intestinal segments of male and female F/F (n = 29) and littermate  $A^{\Delta CD4}$  (n = 28) mice after an oral challenge of olive oil containing [ $^3H$ ]triolein (18:1) for 2 hours. Data are pooled from at least three independent experiments. ( $\mathbf{E}$ ) Total radioactivity in SI from experiments in (D), separated by sex (female, n=14 and 15 mice per group; male, n=15 and 13 mice per group). ( $\mathbf{F}$ ) Kinetics of radioactivity in plasma of F/F (n = 25) and littermate  $A^{\Delta CD4}$  mice (n = 23) after an oral challenge of olive oil containing [ $^3H$ ]triolein (18:1). (**G** and **H**) Radioactivity in heart [(G), n=13 mice per group) and liver [(H), n=10 mice per group] from F/F and littermates  $A^{\Delta CD4}$  after an oral challenge of olive oil containing [ $^3$ H]triolein (18:1) for 2 hours. Data are pooled from at least two independent experiments. (I) Confocal immunofluorescence imaging of neutral lipid accumulation (marked by LipidTOX-Red) in jejunum cross sections from F/F and littermate  $A^{\Delta CD4}$  mice after an oral challenge of olive oil for 2 hours; scale bars are 200  $\mu$ m. The insets show villi tips in higher magnification; scale bars are 50  $\mu$ m. Shown on the right are the mean lipid droplet (LD) size and the total number of LDs per image. n = 5 mice per group pooled from two independent experiments. (J) Body weight of male (left) and female (right) F/F and littermate  $A^{\Delta CD4}$  mice fed ad libitum with 60 kcal% HFD for 9 to 10 weeks (male, n = 17 and 16 mice per group; female, n = 15 mice per group). Data are pooled from at least three independent experiments. (K and L) Fecal nonesterified fatty acid (NEFA) (K) and total cholesterol (L) levels from F/F and littermate  $A^{\Delta CD4} \text{ mice fed ad libitum with HFD for 10 days. } n = 8 \text{ to 11 mice per group. Data are pooled from two independent experiments. For all panels, data are shown as mean} \pm \text{SEM}.$ For (A) to (D), (F), and (J), data points indicate mean values; for (E), (G) to (I), (K), and (L), data points indicate individual mice. The statistical analyses used are as follows: for (A) to (D), two-way analysis of variance (ANOVA) with Sidak's multiple comparison test; for (E), two-way ANOVA; for (F) and (G), repeated measure two-way ANOVA with Sidak's multiple comparison test; and for (G) to (I), (K), and (L), two-tailed unpaired Welch's t test. ns, not significant (p > 0.05); \*p < 0.05; \*\*p < 0.01; \*\*\*\*p < 0.001.

Science 9 OCTOBER 2025 2 of 21

To examine whether T cell-intrinsic Aster-A affected fatty acid uptake by the SI, we gavaged  $A^{\Delta CD4}$  or littermate F/F mice with  $[^3H]$  triolein.  $A^{\Delta CD4}$  mice showed lower peak  $^3H$  uptake in the duodenum and jejunum and reduced total intestinal  $^3H$  absorption after 2 hours (Fig. 1D) in both males and females (Fig. 1E and fig. S3A). Moreover, the magnitude of the reduction was comparable to that observed in  $A^{-/-}$  mice (Fig. 1A).  $A^{\Delta CD4}$  mice also exhibited a reduced rate of  $^3H$  appearance in plasma as well as lower  $^3H$  uptake in heart and liver (Fig. 1, F to H). In line with the radiotracer data, an oral challenge of unlabeled olive oil (of which triolein is a major constituent) resulted in lower total plasma triglyceride levels in  $A^{\Delta CD4}$  mice (fig. S3B). Thus, T cell–specific Aster-A deletion reduced the rate of fatty acid uptake into intestinal epithelium and subsequent entry into the systemic circulation.

We did not observe a difference in the SI length or in gastrointestinal transit times between F/F and  $A^{\Delta CD4}$  mice fed a chow diet (fig. S3, C and D). Histopathology and EM studies revealed that jejunal villus and crypt morphology, villus length, and brush border morphology were indistinguishable in F/F and  $A^{\Delta CD4}$  mice (fig. S3, E and F). No evidence of inflammation was observed in the lamina propria (LP) (fig. S3E). After olive oil gavage, villus tip enterocytes contained large unilocular lipid droplets in F/F mice compared with markedly smaller sized droplets in  $A^{\Delta CD4}$  mice (fig. S3, E and F). We quantified the size and distribution of enterocyte lipid droplets by image analysis of large cross sections of jejunum stained with a neutral lipid probe.  $A^{\Delta CD4}$  mice exhibited a shift in distribution to smaller droplet size and fewer numbers of lipid droplets (Fig. 1I and fig. S3G), accompanied by reduced expression of lipid droplet-associated gene expression in jejunal epithelium (fig. S3H). Furthermore, mice that harbored the CD4<sup>Cre</sup> allele but were heterozygous for the floxed Aster-A allele (CD4-Cre; A<sup>F/+</sup>) showed no difference in [3H]triolein uptake compared with A<sup>F/+</sup> littermates (fig. S4, A to C), thereby confirming that reduced fatty acid uptake in  $A^{\Delta CD4}$  mice was linked to loss of Aster-A function in T cells and not to the presence of CD4<sup>Cre</sup> transgene. Furthermore, uptake of [14C]cholesterol was comparable between F/F and  $A^{\Delta CD4}$  mice (fig. S4, D and E). Thus, the impact of Aster-A in T cells on nutrient absorption was specific to fatty acid uptake and unrelated to any apparent SI pathology.

# Resistance to diet-induced obesity in mice with Aster-A-deficient T lymphocytes

To understand the long-term metabolic impact of Aster-A loss in T cells, we challenged mice with a high-fat diet (HFD). Compared with F/F littermates, both female and male  $A^{\Delta CD4}$  mice were resistant to HFD-induced weight gain (Fig. 1J). After 10 weeks of HFD,  $A^{\Delta CD4}$  mice showed comparable body length to, but were phenotypically leaner than, F/F controls (fig. S5A). Tissue weights of liver, epididymal white adipose tissue, and inguinal white adipose tissue were lower in  $A^{\Delta CD4}$  mice than in controls (fig. S5B). Analysis of body composition by magnetic resonance imaging (MRI) showed less fat mass in  $A^{\Delta CD4}$  mice but no difference in lean mass (fig. S5, C and D). There were no body composition differences when mice were fed a normal chow diet (fig. S5E). Thus, T cell–specific loss of Aster-A conferred resistance to diet-induced obesity.

Loss of Aster-A in T cells blunted the inflammatory adipose tissue changes characteristic of obesity. Histological examination showed comparable fat cell size but reduced macrophage infiltration in epididymal white adipose tissue of HFD-fed  $A^{\Delta CD4}$  mice (fig. S5F). Compared with F/F controls,  $A^{\Delta CD4}$  mice were resistant to adipose resident macrophage (F4/80<sup>hi</sup>CD11b<sup>int</sup>) loss and showed less accumulation of inflammatory macrophages (F4/80<sup>int</sup>CD11b<sup>hi</sup>) (fig. S5, G and H). Furthermore,  $A^{\Delta CD4}$  mice had reduced fat deposition in the liver (fig. S6A) and maintained better glucose tolerance and insulin sensitivity when fed HFD but not when fed a normal chow diet (fig. S6, B to E).

Lower adiposity in  $A^{\Delta CD4}$  mice could not be attributed to differences in food intake, respiratory exchange ratio, or energy expenditure (fig. S7,

A to C). However, with HFD feeding,  $A^{\Delta CD4}$  mice showed increased fecal nonesterified fatty acids compared with controls (Fig. 1K), despite similar total fecal output and abundance of unabsorbed fecal cholesterol (Fig. 1L and fig. S7D). These results indicated overall reduced dietary fat absorption, in addition to altered uptake kinetics. Fecal triglyceride content and pancreatic lipase expression were similar between F/F and  $A^{\Delta CD4}$  mice (fig. S7, E and F). We concluded that loss of Aster-A in T cells decreased intestinal fatty acid uptake, leading to resistance to obesity.

#### Loss of Aster-A in T cells enhances the T<sub>H</sub>17 signature in the SI

Because loss of Aster-A in T cells affected SI fat absorption, we performed transcriptional profiling of CD4<sup>+</sup> and CD8<sup>+</sup> T cells from jejunal LP of mice that were acutely fed olive oil. Although few transcriptional changes related to T cell effector function were observed in the CD8<sup>+</sup> T cells (fig. S8A), genes that were up-regulated and enriched in  $A^{\Delta CD4}$ CD4<sup>+</sup> T cells included Il17a, Il17f, and Il22, which encode the cytokines interleukin-17a (IL-17a), IL-17f, IL-22, respectively, and other genes previously associated with gut T helper 17 (T<sub>H</sub>17) lineage and function (Fig. 2, A to C). We analyzed T cell lineage and cytokine producer frequencies in secondary lymphoid organs and SI-LP of normal chowfed mice and found an increased frequency of IL-17A<sup>+</sup> and IL-22<sup>+</sup> CD4 T cells in mesenteric lymph nodes (mLNs) and SI-LP, respectively (fig. S8, B to E). By contrast, tissue residency markers and frequencies of other T cell lineages were largely unaltered (fig. S8F). Among T helper cell subtypes, Aster-A transcripts (Gramdla) were prominently expressed in the T<sub>H</sub>17 and regulatory T (T<sub>reg</sub>) lineages in mice (Fig. 2D) and in T<sub>H</sub>17 cells in humans (fig. S9, A and B). Aster-A protein levels were most abundant in T<sub>H</sub>17 cells generated in vitro in the presence of IL-1β and IL-23 (fig. S9C), and they increased over the course of differentiation (fig. S9, D and E). The preferential expression of Aster-A in T<sub>H</sub>17 cells corresponded with the predicted binding of transcription factors that enforce the T<sub>H</sub>17 lineage, including JUN, STAT3, EGR2, and SMAD4, at the promotor region of Gramd1a (fig. S9F).

#### Aster-A modulates the accessible cholesterol pool in T<sub>H</sub>17 cells

Aster proteins mobilize the accessible pool of cholesterol from the PM to the ER in several cell types (6, 12, 15, 20). To determine whether Aster-A modulated PM cholesterol levels in T cells, we differentiated primary  $T_H17$  cells from F/F or  $A^{\Delta CD4}$  mice in defined serum-free media to limit extracellular cholesterol availability (fig. S10A) and monitored accessible cholesterol levels on the PM with the ALOD4 probe (3).  $A^{\Delta CD4}$   $T_H17$  cells, but not naïve T cells, exhibited elevated accessible PM cholesterol compared with F/F controls (Fig. 2, E and F, and fig. S10B). Accessible cholesterol was distributed at "hot spots" on F/F  $T_H17$  cells but was widely distributed on the PM of  $A^{\Delta CD4}$   $T_H17$  cells, which resembled T cells forcibly loaded with exogenous cholesterol (Fig. 2G).

To test whether Aster-A contributed to membrane cholesterol homeostasis in the T<sub>H</sub>17 lineage in vivo, we generated mixed bone marrow chimeric mice using F/F or  $A^{\Delta CD4}$  donor and the congenic, wild-type (WT) CD45.1+ competitor (Fig. 2H). This scheme allowed us to conduct an intrinsic comparison of the PM accessible cholesterol pool between Aster-A-sufficient and -deficient SI-LP CD4 T cells using a combination of ALOD4 and surface-marker staining (Fig. 2H). ALOD4 levels on  $A^{\Delta CD4}$  ROR7t<sup>+</sup>  $T_{\rm H}17$  cells were increased compared with that of the CD45.1+ competitor (Fig. 2I). By contrast, no difference was observed between F/F T<sub>H</sub>17 cells and the competitor or in RORyt non-T<sub>H</sub>17 cells between any donor genotypes (Fig. 2I and fig. S10C). Thus, Aster-A regulated accessible cholesterol levels in SI T<sub>H</sub>17 cells in a cell-intrinsic manner. Aster-A deficiency had no effect on RORyt<sup>+</sup> frequency in SI-LP T cells in the mixed bone marrow chimera setting (fig. S10D), consistent with our observations in steadystate mice (fig. S8E). Aster-A-mediated nonvesicular cholesterol transport was thus required to maintain PM cholesterol homeostasis in T<sub>H</sub>17 cells in vitro and in vivo.

Science 9 OCTOBER 2025 3 of 21

Science 9 OCTOBER 2025 4 of 21

# TCR activation generates accessible PM cholesterol and recruits Aster-A

To investigate the physiological signals that modulated accessible cholesterol, we examined PM dynamics in  $T_H17$  cells after TCR activation by plate-bound anti-CD3 and anti-CD28. Control  $T_H17$  cells maintained constant accessible cholesterol levels over 4 hours (Fig. 3A). Aster-Adeficient  $T_H17$  cells exhibited elevated ALOD4 binding after activation, followed by a delayed rate of cholesterol removal (Fig. 3A). TCR-independent activation with phorbol 12-myristate 13-acetate (PMA) and ionomycin, by contrast, led to prolonged and unresolved accessible cholesterol accumulation in  $T_H17$  cells of both genotypes (Fig. 3A). This finding indicated that T cell activation increased accessible PM cholesterol and that Aster-A was required for the normalization of PM cholesterol after TCR activation.

Aster proteins are recruited to the PM by accessible cholesterol (5, 6, 10, 12, 19). To test whether TCR activation was sufficient to recruit Aster-A to the PM, we expressed mCherry fused to the N-terminal GRAM domain of murine Aster-A in the EL-4 mouse T cell line. After synchronized TCR activation, the mCherry signal rapidly mobilized from perinuclear ER toward cell-surface TCRs (Fig. 3B and movie S1), indicating Aster-A recruitment to the PM. Ionomycin further provoked synchronized localization of the mCherry signal to the PM (Fig. 3B and movie S1).

To further resolve the kinetics, we used a dimerization-dependent fluorescent protein (ddFP) system composed of a high-sensitivity GRAM domain (B-GRAM-H) and a PM anchor fused to split fluorescent protein (30, 31), allowing simultaneous detection of accessible cholesterol generation and GRAM recruitment to the PM (Fig. 3C). B-GRAM-H-ddFP was expressed in the EL-4 T cell line and the human Jurkat T cell line (fig. S11A), and ddFP dimerization was detected using flow cytometry. Jurkat cells, but not EL-4 cells, showed increased ddFP signal in response to PM cholesterol loading and thus were used for subsequent experiments (fig. S11B). When Jurkat cells were activated by TCR crosslinking, the ddFP signal increased by 3 min after activation (Fig. 3D) and remained elevated for up to 1 hour (Fig. 3E). Ionomycin treatment led to a larger increase in ddFP signal (Fig. 3F), tracking with a greater accumulation of the PM accessible cholesterol compared with TCR activation (Fig. 3A). These observations prompted us to explore whether a common mechanism altered PM cholesterol distribution during TCRdependent and -independent activation.

Redistribution of cholesterol from the outer to inner leaflet of the PM, which enables sensing and transport by the Asters, can be triggered by altered transmembrane phospholipid asymmetry (32), such as phosphatidylserine (PS) scrambling. TCR-mediated activation triggers nonapoptotic, low-grade, and reversible PS flipping to the PM outer leaflet, in contrast to ionomycin, which generates persistent widespread PS scrambling (33–35). We confirmed these prior findings in primary T<sub>H</sub>17 cells, Jurkat cells, and EL-4 cells using Annexin-V detection of outer leaflet PS (fig. S12A). We further tested whether TCR activation– or ionomycin-induced GRAM recruitment depends on TMEM16F, a major Ca<sup>2+</sup>-dependent PS scramblase (36). 1PBC, a well-characterized TMEM16F inhibitor (37), eliminated the ionomycin-induced Annexin-V-high population, but the Annexin-V-low population induced by both TCR activation and ionomycin appeared to be

TMEM16F independent (fig. S12, B and C). Accordingly, 1PBC largely abolished ionomycin-induced, but not TCR-induced, GRAM recruitment (fig. S12, D and F, and quantified in fig. S12, E and G). Thus, both TCR-dependent and -independent T cell activation generated accessible cholesterol and recruited Aster proteins to the PM, and TMEM16F-mediated PS scrambling contributed to this phenomenon upon ionomycin exposure.

# Aster-A restrains TCR nanoclustering and dampens proximal TCR signaling

PM cholesterol composition has been proposed to modulate membrane TCR activity and avidity by affecting TCR nanoclustering (22, 38). We tested whether loss of Aster-A affected the accessible and SM-sequestered cholesterol pools using ALOD4 and OlyA probes, respectively (4).  $\rm A^{\Delta CD4}\,T_{H}17$  cells showed enhanced ALOD4 and OlyA binding to the PM compared with F/F  $\rm T_{H}17$  cells at steady state, and both pools expanded upon TCR activation (Fig. 3G). These data suggested that excess accessible PM cholesterol in Aster-A-deficient cells funneled into SM-sequestered domains.

We investigated whether the accumulation of accessible and SM-sequestered PM cholesterol in  $A^{\Delta CD4}$   $T_H17$  cells altered TCR nanoclustering or signaling. Serial extraction of isolated  $T_H17$  membranes by saponin and Brij97 allowed separation of nanoclustered complexes from monomeric TCR (*39*). Quantification of CD3 $\zeta$  chain abundance in these fractions indicated that the loss of Aster-A increased the TCR nanocluster-to-monomer ratio (Fig. 4, A and B). Accordingly, after reactivation,  $A^{\Delta CD4}$   $T_H17$  cells exhibited enhanced proximal TCR signaling, as well as increased phosphorylation of S6 and ERK, compared with control  $T_H17$  cells (Fig. 4C and quantified in fig. S13A). Consequently,  $A^{\Delta CD4}$   $T_H17$  cells showed increased frequency of IL-17A and IL-22 effector cytokine production and gene expression, reduced Foxp3 expression (Fig. 4, D and E), and a moderate increase in proliferation (fig. S13B). We conclude that Aster-A functions to restrain TCR nanoclustering and signaling in  $T_H17$  cells by removing PM cholesterol.

To understand whether this pathway operated in vivo, we intraperitoneally administered CD3 $\epsilon$ -specific antibody to mice (Fig. 4F), a challenge that elicits activation and expansion of mLN- and intestine-associated  $T_H17$  cells (fig. S13C) (40). After anti-CD3 $\epsilon$  injection, ALOD4 staining of F/F mLN T cells showed unchanged accessible cholesterol levels at 8 hours and a moderate increase at 24 hours (Fig. 4G). By contrast, accessible PM cholesterol accumulated substantially in  $A^{\Delta CD4}$  mLN T cells 8 to 24 hours after injection (Fig. 4G). Furthermore, anti-CD3 $\epsilon$  treatment markedly expanded ROR $\gamma$ t<sup>+</sup> CD4 T cells in the mLNs of  $A^{\Delta CD4}$  mice at 24 hours, consistent with our finding that Aster-A dampens  $T_H17$  reactivation (Fig. 4H). These data demonstrated that TCR activation led to increased PM accessible cholesterol and that Aster-A is required for its timely removal to limit  $T_H17$  activation and expansion.

#### Spatial association of Aster-A with STIM1 in T cells

To gain further insight into mechanisms by which Aster-A modulates T cell function, we probed the Aster-A proximity interactome by harnessing TurboID fused to the N terminus of Aster-A (fig. S14A) (41). This fusion allowed identification of proteins proximal to Aster-A after

Science 9 OCTOBER 2025 5 of 21

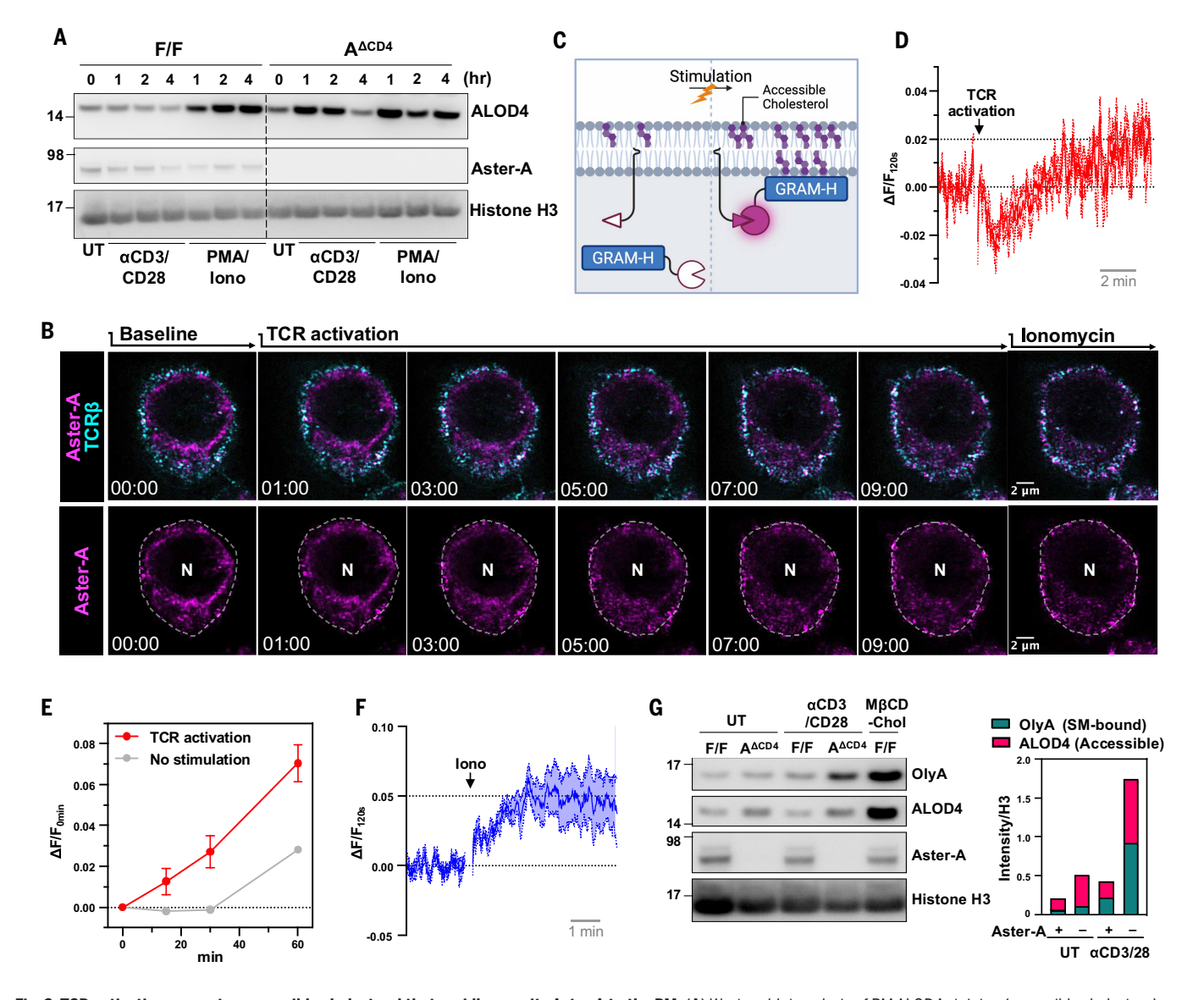


Fig. 3. TCR activation generates accessible cholesterol that rapidly recruits Aster-A to the PM. (A) Western blot analysis of PM ALOD4 staining (accessible cholesterol level) of invitro-differentiated F/F and  $A^{\Delta CD4}$  pT<sub>H</sub>17 cells (IL-6 + TGF $\beta$  + IL-1 $\beta$  + IL-23) that were reactivated with plate-bound anti-CD3/CD28 antibody (1 µg/ml) for the indicated times. UT, untreated. (B) Live-cell confocal microscopy images showing the localization of mCherry-Aster-A in EL-4 cells unstimulated (Baseline), TCR cross-linked, or treated with 1 µM ionomycin. PM TCR $\beta$  was stained with anti-TCR $\beta$ -Alexa Fluor 647 antibodies. Scale bars are 2 µm. N, nucleus. (C) Schematic graph of PM recruitment-dependent B-GRAM-H ddFP dimerization. (D) Time course of ddFP fluorescence signal (normalized to the first 120 s of baseline signal) in response to TCR cross-linking. Shown is a trace of four independent recordings, with an average of 200 to 1000 cells per second per recording. (E) Kinetics of ddFP signal in a 60-min timescale. n = 4 independent recordings for TCR activation. (F) Time course of ddFP fluorescence signal (normalized to first 120 s of baseline signal) in response to 1 µM ionomycin. Shown is a trace of five independent recordings, with an average of 200 to 1000 cells per second per recording. (G) Western blot analysis of ALOD4 (accessible cholesterol level) and OlyA (SM-sequestered cholesterol level) staining of invitro-differentiated F/F and  $A^{\Delta CD4}$  T<sub>H</sub>17 cells (IL-6 + TGF $\beta$  + IL-1 $\beta$  + IL-23) that were reactivated with plate-bound 1 µg/ml anti-CD3/CD28 antibody or loaded with 25 µM methyl- $\beta$ -cyclodextrin-cholesterol (M $\beta$ CD-Chol) for 1 hour. Data are representative of or pooled from at least two independent experiments. Data are shown as mean  $\pm$  SEM. [(C) created with BioRender.com]

its recruitment to the PM by cholesterol loading or TCR activation (Fig. 5A). Excess PM cholesterol induced Aster-A self-biotinylation (Fig. 5B and fig. S14B), consistent with the reported oligomerization of Aster-A at PM-ER contact sites (12, 19). Our screen revealed stromal interaction molecule 1 (STIM1)—a core component of the store-operated  ${\rm Ca}^{2+}$  entry (SOCE) machinery and known PM-ER contact site protein (42-46)—to be in proximity to Aster-A. Aster-A association with STIM1 increased after both cholesterol loading (Fig. 5B and fig. S14B) and TCR activation (lane 3 in Fig. 5C). This association was enhanced by  ${\rm Ca}^{2+}$  chelators that prolong STIM1 localization at PM-proximal ER (lane 4 in Fig. 5C) (47, 48). Despite only pulling down a small fraction of

endogenous or overexpressed STIM1 with Aster-A, their coimmuno-precipitation was nevertheless increased upon cholesterol loading (fig. S14, C and D). These data implied that Aster-A and STIM1 interacted transiently rather than forming a stable complex. By contrast, the intracellular TCR signaling components LCK and CD3e did not show prominent interaction with Aster-A (Fig. 5C), suggesting that TCR nanoclustering in the setting of Aster-A deficiency was largely a result of preexisting PM cholesterol accumulation (Fig. 4A).

Previously identified residues that are required for Aster-B sensing and transfer of PM cholesterol are highly conserved in Aster-A (fig. S15A) (19, 49). Homologous mutations in Aster-A resulted in corresponding

Science 9 OCTOBER 2025 6 of 21

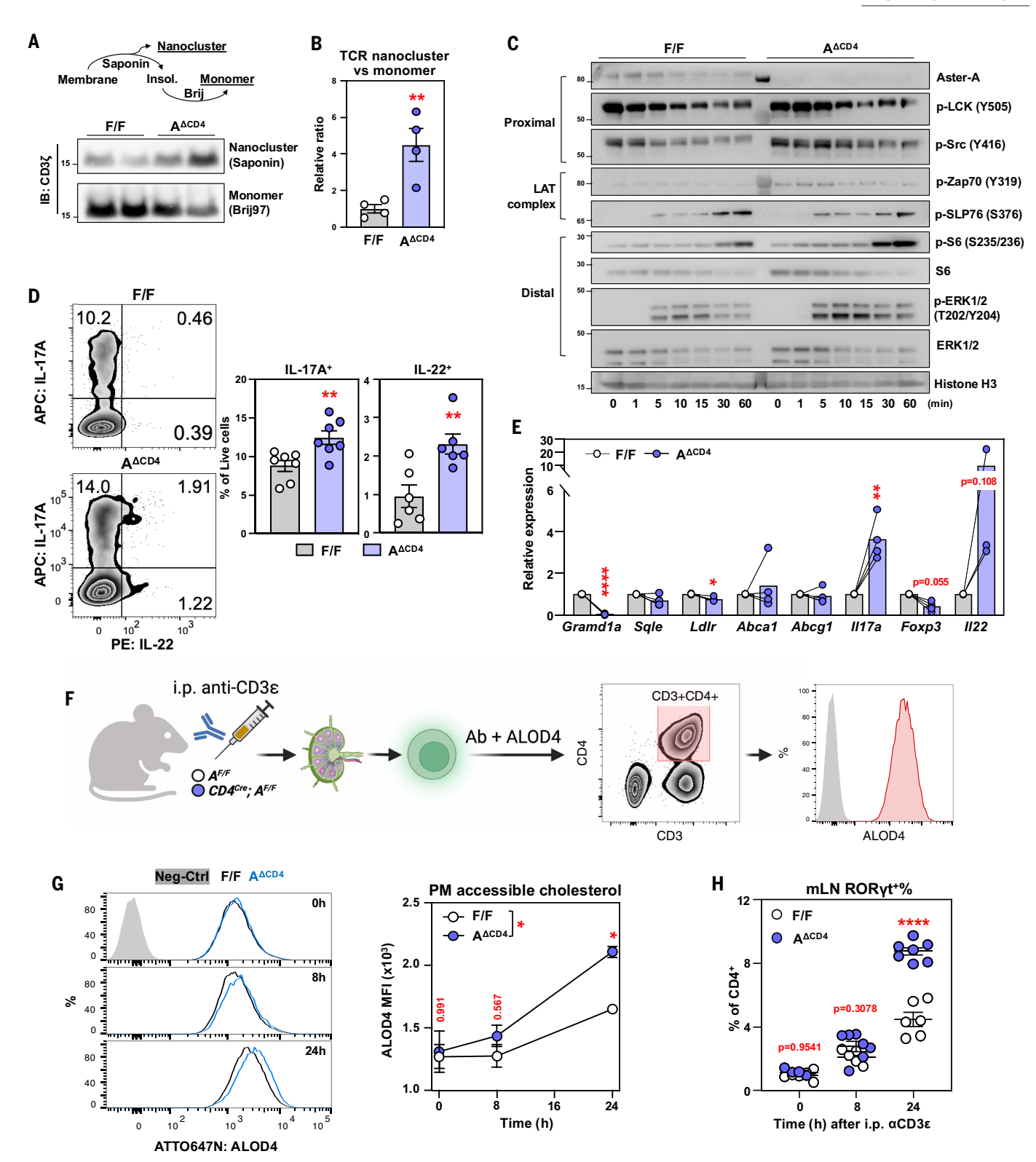


**Fig. 4. Aster-A regulates TCR nanoclustering and effector responses of T<sub>H</sub>17 cells through gating PM cholesterol level. (A and B)** Western blot analysis of TCR (CD3 $\zeta$ ) clustering in invitro—differentiated F/F and A<sup>ΔCD4</sup> pT<sub>H</sub>17 cells (IL-6 + TGF $\beta$  + IL-1 $\beta$  + IL-2 $\beta$ ). Shown are a representative blot (A) showing two biological replicates and a quantification (B) of Saponin-extracted (nanocluster) versus Brij97-extracted (monomer) CD3 $\zeta$  intensity. n = 4 biological replicates from two independent experiments. (**C**) Western blot analysis of phosphorylation of LCK/Src, Zap70, SLP76, S6, and ERK1/2 after TCR activation. Invitro—differentiated pT<sub>H</sub>17 cells were "rested" overnight without a differentiation cocktail or TCR stimulus and then reactivated with plate-bound anti-CD3 and anti-CD28 antibodies (1 μg/ml) for the indicated times. Histone H3 serves as overall input control. Data are representative of three independent experiments. (**D**) Frequency of invitro—differentiated pT<sub>H</sub>17 cells producing IL-17A or IL-22 (gated on live single cells). A representative flow plot is shown on the left, and quantifications are on the right. n = 6 or 7 mice per genotype from at least two independent experiments. (**E**) Gene expression from invitro—differentiated pT<sub>H</sub>17 cells n = 3 or 4 biological replicates per genotype from three independent experiments. (**F**) Diagram of the experimental setup to probe PM

Science 9 OCTOBER 2025 7 of 21

accessible cholesterol levels during T cell activation invivo. i.p., intraperitoneal. **(G)** Shown on the left is a histogram of ALOD4 staining in mLN CD4 T cells (CD45<sup>+</sup>CD3<sup>+</sup>CD4<sup>+</sup>) from F/F and  $A^{\Delta CD4}$  mice that were intraperitoneally injected with anti-CD3 $\epsilon$  (20  $\mu$ g/mouse) for the indicated times or 20  $\mu$ g isotype control antibody (0 hour time point). Shown on the right is the normalized mean fluorescence intensity (MFI) of ATT0647N-ALOD4. n=3 or 4 mice per genotype per time point, representative of two independent experiments. **(H)** Frequency of ROR $\gamma$ t<sup>+</sup> population in mLN CD4<sup>+</sup> T cells at the indicated time points after anti-CD3 $\epsilon$  injection. n=4 to 7 mice per group per time point, pooled from two independent experiments. For (B), (D), (G), and (H), data are shown as mean  $\pm$  SEM. For (A) and (D), data points indicate cells generated from individual mice; for (E), data points and connecting lines indicate cells generated from paired biological replicates; for (G), data points indicate mean values; and for (H), data points indicate individual mice. The statistical analyses used are as follows: for (B) and (D), two-tailed Welsh's t test; for (E), multiple ratio paired t test; and for (G) and (H), two-way ANOVA with Sidak's multiple comparison test. \*p < 0.05; \*\*p < 0.05; \*\*p < 0.001; \*\*\*\*p < 0.0001. [(F) created with BioRender.com]

alterations in PM localization patterns in response to cholesterol loading (fig. S15B). Aster-A R186W, which contains a loss-of-function GRAM domain mutation (Arg<sup>186</sup>→Trp) that diminishes cholesterol sensing capacity, failed to localize to the PM in response to cholesterol (fig. S15B). Coimmunoprecipitation of STIM1 with Aster-A R186W was reduced compared with WT Aster-A (fig. S14D). The observation that the abundant ER-resident protein calnexin did not coimmunoprecipitate with WT Aster-A suggested that recruitment of Aster-A and STIM1 to the PM was required for their association, despite the fact that they are both ER-anchored proteins (fig. S14C). To visualize the localization of Aster-A relative to STIM1, we reconstituted  $A^{\Delta CD4}$  T<sub>H</sub>17 cells with hemagglutinin (HA)-tagged Aster-A (Fig. 5D and fig. S14E). In resting T<sub>H</sub>17 cells, both STIM1 and Aster-A localized primarily to perinuclear ER (row 1 in Fig. 5D). In response to synchronized TCR activation, WT Aster-A migrated to the PM and in proximity to the STIM1 "ring" or "cap" structure (row 2 in Fig. 5D). Aster-A R186W failed to translocate to the PM, but this did not adversely affect STIM1 localization (row 3 in Fig. 5D). Thus, when accessible cholesterol was available on the T cell PM, Aster-A increased its proximity to STIM1 owing to their colocalization at PM-ER contact sites.

# Aster-A and accessible cholesterol regulate TCR-induced ${\rm Ca}^{2+}$ cascades

The coupling of STIM1 with the PM  $Ca^{2+}$  channel ORAI1 (calcium release – activated calcium modulator 1) is indispensable for SOCE and  $T_H17$  effector function (50–52). The association of Aster-A and STIM1 suggested that Aster-A may regulate SOCE in  $T_H17$  cells. Using flow-cytometry and imaging-based assays, we found that  $A^{\Delta CD4}$   $T_H17$  cells showed increased TCR-dependent and ionophore-induced  $Ca^{2+}$  influx, without affecting STIM1 expression (Fig. 5E and fig. S16, A and B). By comparison, Aster-A deficiency did not affect SOCE in naïve T cells (fig. S16, B and C).

We asked whether cholesterol sensing or transport by Aster-A was required for the modulation of SOCE. In addition to Aster-A R186W, we generated and validated two additional homologous mutations: G184L (Gly<sup>184</sup>→Leu), a gain-of-function GRAM domain mutation, which increased Aster-A localization to the PM; and 5P [I431P (Ile<sup>431</sup> → Pro), S432P (Ser<sup>432</sup>→Pro), N433P (Asn<sup>433</sup>→Pro), Q434P (Gln<sup>434</sup>→Pro), L435P (Leu<sup>435</sup>→Pro)], a loss-of-function ASTER domain mutation that is unable to transport cholesterol. 5P was used as a reconstituted but nonfunctional control (fig. S15, A and B). Reconstitution of primary  $A^{\Delta CD4}$  $T_{\rm H}$ 17 cells with WT Aster-A or G184L decreased PM accessible cholesterol and Ca<sup>2+</sup> flux (Fig. 5F and fig. S16, D and E). Conversely, reconstitution with loss-of-function mutations in the GRAM domain (R186W) or ASTER domain (5P) elevated PM accessible cholesterol and Ca<sup>2+</sup> flux (Fig. 5F and fig. S16, D and E). Thus, regulation of Ca<sup>2+</sup> flux required both recruitment of Aster-A to the PM and cholesterol transfer capacity. These data indicate that Aster-A negatively regulated TCR-induced SOCE in  $T_H17$  cells.

Increasing PM cholesterol by treating  $T_H17$  cells with methyl- $\beta$ -cyclodextrin-cholesterol or low-density lipoprotein (LDL) promoted TCR-dependent SOCE, whereas removing PM cholesterol by 2-hydroxypropyl- $\beta$ -cyclodextrin abolished it (fig. S16, F and G). To understand the specific role of the accessible cholesterol pool in STIM1-dependent Ca<sup>2+</sup> flux, we incubated WT  $T_H17$  cells with ALOD4

to sequester and immobilize accessible cholesterol on the outer leaflet of the PM. ALOD4 markedly dampened TCR-induced Ca<sup>2+</sup> flux compared with treatment with the nonbinding mutant (*53*), whereas maximum flux induced by ionomycin was intact (Fig. 5H). Therefore, we propose a model in which accessible cholesterol generated by TCR activation supports SOCE, whereas the recruitment of Aster-A to the proximity of STIM1 curtails Ca<sup>2+</sup> influx by modulating PM cholesterol composition.

Aster proteins are highly conserved in mammals (12). We generated an Aster-A-deficient Jurkat T cell clone by CRISPR-Cas9 and then reconstituted it with human Aster-A or an empty vector (fig. S16H). Stable expression of human Aster-A efficiently reduced both TCR- and ionomycin-triggered  $\text{Ca}^{2+}$  flux compared with empty vector-transduced cells (Fig. 5H), mirroring our observations for mouse  $\text{T}_{\text{H}}$ 17 cells (Fig. 5E). These data revealed a functionally conserved accessible cholesterol-Aster-A/STIM1 axis that regulated  $\text{Ca}^{2+}$  responses in T cells.

#### IL-22 drives malabsorption in T cell Aster-A deficiency

We investigated the basis for dietary lipid malabsorption in  $A^{\Delta CD4}$ mice. To explore factors in SI T<sub>H</sub>17 cells that may affect absorption, we performed single-cell RNA sequencing (scRNA-seq) of SI-LP mononuclear cells. CD90<sup>+</sup> (based on *Thy1* expression, the gene that encodes CD90) clusters were subsequently extracted and further subclustered to reveal 23 distinct lymphocyte subpopulations, including conventional T cell subtypes,  $\gamma\delta$  T cells, innate lymphoid cells, and natural killer T cells (Fig. 6A and fig. S17A). Four prominent RORγt (Rorc)expressing populations were identified, denoting T<sub>H</sub>17 cells (cluster-8),  $ROR\gamma t^{+}T_{reg}$  cells (cluster-7),  $\gamma \delta T$ -17 cells (cluster-14), and type-3 innate lymphoid cells (ILC3, cluster-15) (Fig. 6B and fig. S17A). Examination of cluster-8 revealed that SI-LP  $T_H17$  cells from  $A^{\Delta CD4}$  mice expressed higher levels of Il22, with subtle changes in Rorc and Il17a expression (Fig. 6C and fig. S17B). The expression of other canonical cytokines produced by SI  $T_H17$  cells, such as IL-17f, IL-21, and interferon- $\gamma$ , were either below detection or comparable between genotypes (fig. S17B). Other markers associated with mucosal T<sub>H</sub>17 effector or regulatory functions were not notably changed (fig. S17, C and D).

IL-22 is a mucosal T<sub>H</sub>17-associated cytokine in mice that maintains gut homeostasis and mucosal defense by increasing the production of antimicrobial peptides and promoting epithelial regeneration (54, 55). Consistent with our RNA-seq results (Figs. 2A and 6C), flow cytometry revealed increased IL-22 $^+$  frequency among A $^{\Delta CD4}$  SI-LP CD4 T cells, which also often coexpressed IL-17A (Fig. 6D). We generated F/F and A<sup>ΔCD4</sup> mice harboring an IL-22-GFP reporter allele (GFP, green fluorescent protein). A<sup>ΔCD4</sup> SI-LP CD4<sup>+</sup> T cells were more frequently GFP<sup>+</sup> than SI-LP CD4<sup>+</sup> T cells of control mice (Fig. 6E), whereas the GFP<sup>+</sup> percentages of non-CD4 T cells and innate lymphocytes were comparable (fig. S18A). Induction of gut  $T_{\rm H}17$  cells and IL-22 $^+$  populations in laboratory mice depends on the colonization of segmented filamentous bacteria (SFB) (56). Accordingly, increased IL-22 in  $A^{\Delta CD4}$  mice was mainly attributed to TCR Vβ14<sup>+</sup> T cells, a major clonal response to SFB antigen (Fig. 6E) (57, 58). Thus, loss of nonvesicular cholesterol transport in T<sub>H</sub>17 cells led to increased IL-22-producing cells in SI-LP.

Chronic overexpression or loss of IL-22 alters nutrient metabolism (59-63). We assessed whether exogenous IL-22 could suppress the absorption of a bolus of triolein. A single administration of IL-22

Science 9 OCTOBER 2025 8 of 21

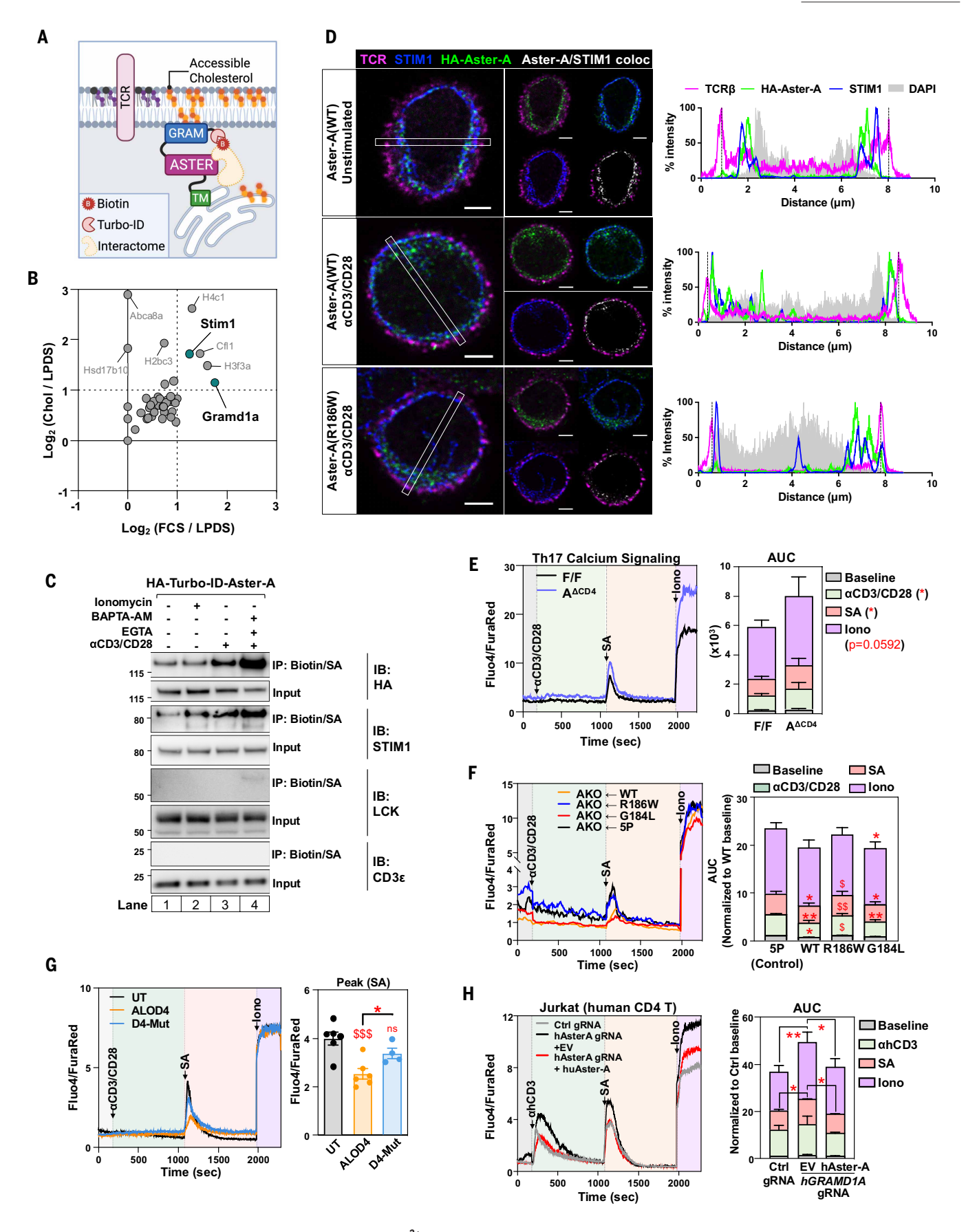


Fig. 5. Aster-A associates with STIM1 and modulates TCR-mediated Ca<sup>2+</sup> signaling. (A) Schematic graph showing the proximal labeling strategy using N-terminal TurbolD-fused Aster-A. (B) Results of semiquantitative proteomics showing differentially biotinylated proteins. EL-4 cells expressing TurbolD-Aster-A were treated with 10%

Science 9 OCTOBER 2025 9 of 21

lipoprotein-deficient serum (LPDS) media overnight, 10% fetal bovine serum (FCS) media overnight, or LPDS media and loaded with 100 μM methyl-β-cyclodextrin-cholesterol (Chol). (C) Western blot analysis of biotinylated proteins in TurboID-Aster-A EL-4 T cells stimulated with ionomycin (1 µM) or plate-bound anti-CD3/CD28 (5 µg/ml) in the presence or absence of BAPTA-AM (50 µM) and EGTA (10 mM) for 1 hour. SA, streptavidin. (D) Immunofluorescence analysis of cellular localization of HA-Aster-A, endogenous STIM1, and PM  $TCR\beta \ in \ primary \ mouse \ T_H17 \ cells. \ A^{\Delta CD4} \ T_H17 \ cells \ were \ reconstituted \ with \ HA-tagged \ WT \ or \ R186W \ Aster-A \ and \ were \ either \ unstimulated \ or \ stimulated \ with \ TCR \ cross-linking$ (soluble 5 µg/ml biotin-anti-CD3 and anti-CD28 followed by 10 µg/ml SA). Shown on the left are merged images of all three or two of the three channels, as well as HA-Aster-A/ STIM1 colocalization (white). Shown on the right are the relative pixel intensities of TCR<sub>B</sub>-Alexa Fluor 647, HA-Alexa Fluor 555, and STIM1-Alexa Fluor 488 from a cross section of the cell (white box). Scale bars are  $2 \mu m$ . (E) Shown on the left are SOCE traces (median of the ratio of  $Ca^{2+}$  indicators Fluo-4 to FuraRed) from F/F and  $A^{\Delta CD4}T_H17$  cells that were  $restimulated \ with \ soluble \ biotin-anti-CD3 \ and \ anti-CD28 \ (5 \ \mu g/ml), \ followed \ by SA-mediated \ cross-linking \ (10 \ \mu g/ml) \ and \ ionomycin \ (1 \ \mu M). \ The \ trace \ is \ the \ average \ from \ n=3 \ and \ restimulated \ and \ restimulated \ and \ restimulated \ restimulated \ and \ restimulated \ restimulated \ and \ restimulated \ restim$ independent experiments. On the right, the area under curve (AUC) of each treatment is quantified. (F) Shown on the left is a representative SOCE trace from Aster-A-deficient (A^CD4) TH17 cells reconstituted with 5P (ASTER domain loss of function, control), WT, R186W (GRAM domain loss of function), or G184L (GRAM domain gain of function) Aster-A. The trace is representative of three independent experiments. On the right, the AUC of each treatment is quantified. The \* represents comparison to 5P mutant; the \$ represents comparison to WT. n = 5 independent experiments. The gating strategy is shown in fig. S22. (G) Shown on the left is a representative SOCE trace from WTT<sub>H</sub>17 cells restimulated as (E). Cells were treated with 20 µg/ml purified ALOD4 or the cholesterol nonbinding mutant (D4-Mut) 30 min before time 0. Shown on the right are quantifications of peak SOCE. n = 4 to 6 independent experiments. The \$ represents comparison to the untreated condition. (H) Shown on the left is a representative SOCE trace from Ctrl guide RNA (gRNA) or Aster-A knockout (GRAMD1A gRNA) human Jurkat T cell clones reexpressed with empty vector (EV) or human Aster-A. On the right, the AUC of each treatment is quantified. n = 3 independent experiments. In (E) to (H), data are shown as mean  $\pm$  SEM. For (G), data points indicate independent experimental replicates. The statistical analyses used are as follows: for (E), paired two-way ANOVA with Sidak's multiple comparison test; for (F) and (H), multiple paired one-way ANOVA with Tukey's multiple comparison test; and for (G), ordinary one-way ANOVA. ns, not significant (p > 0.05); \*p or \$p < 0.05; \*\*p or \$p < 0.05; \*p < 0

for 1 hour before [ $^3$ H]triolein challenge markedly reduced radiolabel uptake across the length of the SI and its subsequent appearance in circulation (Fig. 6, F and G, and fig. S18B). To determine whether increased IL-22 production from  $A^{\Delta CD^4}$   $T_H$ 17 cells affected SI epithelial homeostasis, we assessed signaling and transcriptional components downstream of the IL-22 receptor. Jejunal epithelial scrapings from  $A^{\Delta CD^4}$  mice showed elevated STAT3 phosphorylation compared with scrapings from controls in both fasted and oil-fed states (Fig. 6H), confirming that IL-22 signals to jejunal epithelium, where most dietary fatty acids are absorbed. Furthermore, the distal ileum of  $A^{\Delta CD^4}$  mice showed elevated expression of IL-22–responsive antimicrobial peptides, regenerating islet-derived protein (Reg)  $3\beta$  and Reg3 $\gamma$  (fig. S18C). Thus, the consequences of increased IL-22 production from  $A^{\Delta CD^4}$   $T_H$ 17 cells were evident throughout the length of the SI.

To directly test the hypothesis that elevated IL-22 contributed to lower fatty acid uptake in  $A^{\Delta CD4}$  mice, we transiently blocked the effect of IL-22 with a neutralizing antibody (Fig. 61). IL-22 neutralization effectively lowered Reg3b and Reg3g expression in  $A^{\Delta CD4}$  mice compared with mice administered control isotype immunoglobulin G (IgG) (fig. S18C). Notably, blocking IL-22 also reversed the impairment of fatty acid absorption in  $A^{\Delta CD4}$  mice (Fig. 6J). To further determine the contribution of T cell IL-22 to diet-induced obesity in  $A^{\Delta CD4}$  mice, we generated  $Il22^{F/F}A^{F/F}CD4^{Cre}$  and  $Il22^{F/F}A^{F/F}$  mice (fig. S19A).  $Il22^{F/F}A^{F/F}CD4^{Cre}$  and  $Il22^{F/F}A^{F/F}$  mice showed no difference in weight gain when challenged with HFD (fig. S19B). SI [ $^3$ H]triolein uptake was also normalized between the two genotypes (fig. S19C), thus implicating the epistatic relationship between IL-22 and Aster-A in T cells. These data indicated that loss of Aster-A in T cells decreased fatty acid absorption and restrained diet-induced obesity via IL-22.

Gut-resident immune cells and IL-22 can influence the microbiota composition (63, 64), which may independently affect responses to diet (65, 66). However, F/F and  $A^{\Delta CD4}$  mice fed HFD had similar fecal bacterial composition (fig. S20A). Depletion of gut bacteria and fungus with broad spectrum antibiotics effectively reduced Il22 transcripts in SI and mLNs (fig. S20, B to D) and accordingly restored fatty acid uptake in  $A^{\Delta CD4}$  mice (fig. S20, E and F). Furthermore, littermate F/F and  $A^{\Delta CD4}$  mice that were individually housed or cohoused to either deviate or normalize microbiota showed similar differences in HFD-induced weigh gain and fat mass (fig. S20, G and H). Thus, the gut microbiota was required for IL-22 induction but itself did not directly contribute to impaired fatty acid uptake in  $A^{\Delta CD4}$  mice. We conclude that the effect of T cell–specific loss of Aster-A changes fatty acid absorption through direct T cell–enterocyte communication mediated by IL-22.

#### **Discussion**

Aster proteins are recruited to PM-ER contact sites by accessible cholesterol and mobilize this pool to the ER (12). Here, we showed that the accessible PM cholesterol pool expands immediately after TCR activation, leading to Aster-A recruitment. Some of this additional accessible cholesterol, if not removed promptly, appeared to be funneled into the SM-sequestered domains (21, 22), which supported TCR nanoclustering and reduced the threshold for activation. We posit that the heightened  $T_{\rm H}17$  effector function observed in vitro and in vivo in the absence of Aster-A arises from both the inability to rapidly remove accessible cholesterol generated by TCR activation and the increased abundance of TCR nanoclusters formed as a result of chronic accumulation of SM-cholesterol domains.

Excess ER free cholesterol is rapidly converted to cholesteryl esters by acyl-coenzyme A:cholesterol acyltransferases (ACATs) (67). Inhibition of ACAT1 causes PM cholesterol accumulation and potentiates TCR activity in cytotoxic T cells (25, 68). Our results in  $T_{\rm H}17$  cells suggest that Asters most likely act upstream of ACATs in this regulatory axis. Loss of Aster-A alone does not seem to affect peripheral T cell composition, consistent with previous studies in which homeostatic T cell cholesterol content was perturbed by loss of SCAP/SREBP2, ACAT1, or SULT2B1B (21, 25, 69, 70). Instead, PM cholesterol accumulates in Aster-A-deficient SI-LP  $T_{\rm H}17$  cells in a cell-autonomous manner. Dynamic expansion of the accessible cholesterol pool also occurred after T cell activation and was associated with the expansion of Aster-A-deficient ROR $\gamma$ t<sup>+</sup>  $T_{\rm H}17$  cells in vivo. Thus, we propose that Aster-A is an indispensable guard of  $T_{\rm H}17$  membrane homeostasis.

It was unknown whether Asters cooperate with other classes of membrane contact-site proteins at the PM. We identified the proximity of Aster-A with STIM1 in activated T cells. The precise molecular details by which Aster-A affects STIM1 function in SOCE remain to be determined. Notably, two unbiased protein interaction and proximity maps also identified the association of Aster-A with STIM1 and TCR components (71, 72). Prior microscopy studies in human epithelial and fibroblast cell lines suggested stable colocalization of STIM1 with GRAMD2A, but not GRAMD1A (encoding human Aster-A), at PM-ER contact sites (73). Given that we failed to coimmunoprecipitate a substantial quantity of STIM1 with Aster-A, we posit that their interaction is likely transient or indirect. Furthermore, murine T cells show only trace expression of Gramd2, suggesting that STIM1-containing PM-ER contact sites must be defined by a different set of proteins in T cells. Recruitment of the Aster GRAM domain to the PM requires dual recognition of accessible cholesterol and anionic phospholipids such as PS (5, 10, 12, 19, 49, 74). Paradoxically, PS scrambling from the inner to outer leaflet appears to contribute to ionomycin-induced

Science 9 OCTOBER 2025 10 of 21

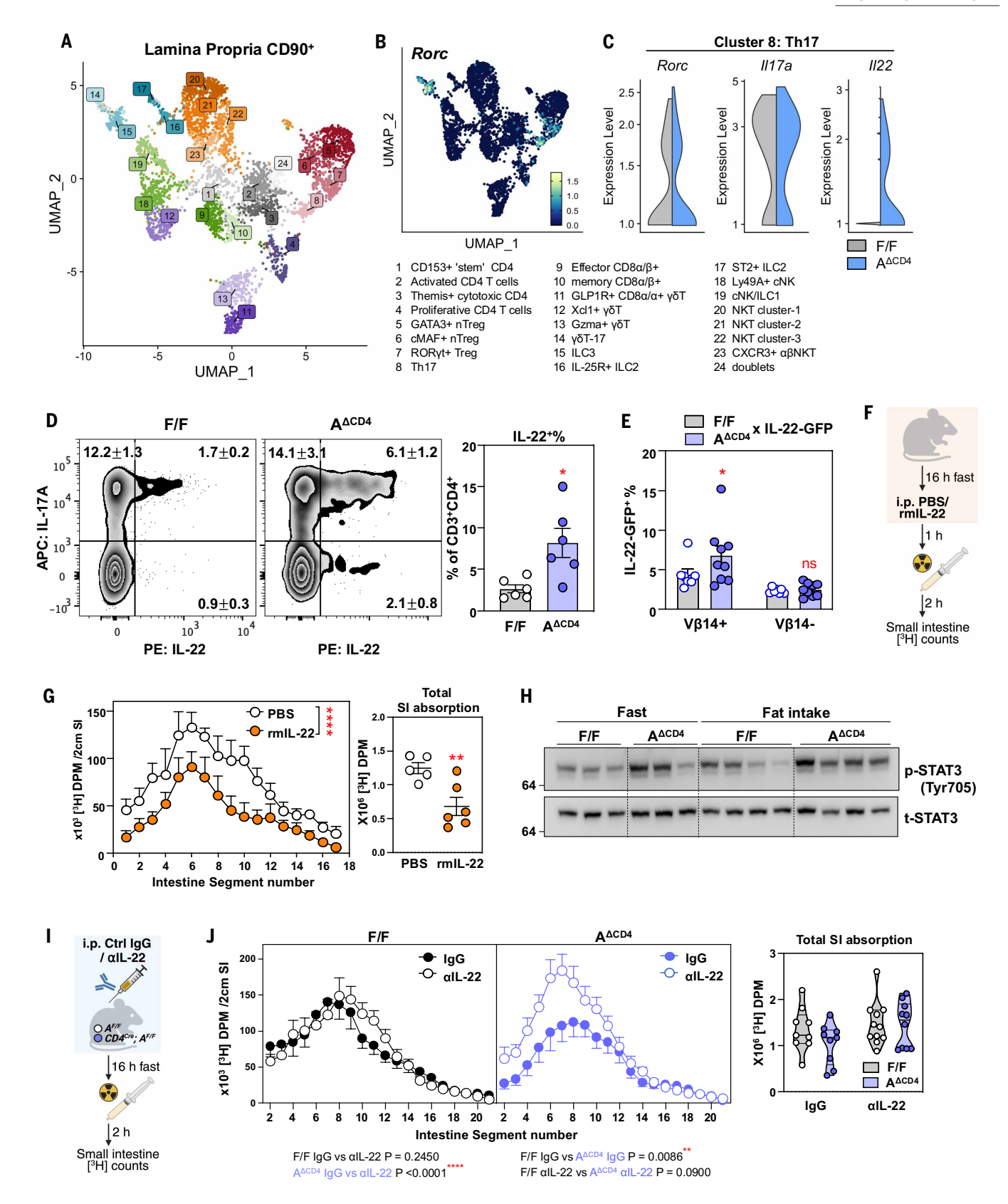


Fig. 6. Aster-A deficiency leads to IL-22-mediated inhibition of fatty acid absorption. (A) Uniform manifold approximation and projection (UMAP) analysis of scRNA-seq data from SI-LP CD90<sup>+</sup> (based on *Thy1* expression) cells from F/F and littermate  $A^{\Delta CD4}$  mice. Cluster annotations are listed at the bottom right. n=1 biological replicate pooled from three mice per group (total of 4239 cells in UMAP). (B) UMAP analysis of *Rorc* expression. (C) Violin plots of *Rorc*, *Il17a*, and *Il22* expression in cluster-8 (T<sub>H</sub>17) cells from scRNA-seq analysis in (A) and (B). (D) Representative flow plots of IL-17A<sup>+</sup> and IL-22<sup>+</sup> SI-LP T cells (CD45<sup>+</sup>CD3<sup>+</sup>CD4<sup>+</sup>) from F/F and littermate  $A^{\Delta CD4}$  mice gavaged with olive oil for 2 hours. Quantified percentages are shown on the right. n=6 mice per group, pooled from two independent experiments. The gating strategy is shown in fig. S24A. (E) Percentage of IL-22-GFP<sup>+</sup> in Vβ14<sup>+</sup> or Vβ14<sup>-</sup> SI-LP T cells (CD45<sup>+</sup>CD90<sup>+</sup>CD3<sup>+</sup>CD4<sup>+</sup>) from Aster- $A^{F/F}$  Il22<sup>GFP</sup>(F/F x IL-22-GFP) and littermates Aster- $A^{F/F}$  CD4<sup>Cre</sup> Il22<sup>GFP</sup>(A<sup>ΔCD4</sup> x IL-22-GFP)

Science 9 OCTOBER 2025 11 of 21

#### **RESEARCH ARTICLE**

mice gavaged with olive oil for 2 hours. n=7 to 9 mice per group, pooled from two independent experiments. The gating strategy is shown in fig. S24B. (**F**) Schematic diagram for the IL-22 treatment experiment in (G). (**G**) Shown on the left is the distribution of radioactivity in SI segments of C57/BL6J WT mice after an oral challenge of olive oil containing [ $^3$ H]triolein (18:1) for 2 hours. Mice were intraperitoneally injected with phosphate-buffered saline (PBS) or 1.5  $\mu$ g IL-22 at 1 hour before triolein challenge. Shown on the right is the total radioactivity in the SI. n=5 or 6 mice per group, representative of two independent experiments. (**H**) Western blot analysis of phospho-STAT3 (tyrosine 705) and total STAT3 (t-STAT3) in jejunal epithelial scrapings from F/F and littermate  $A^{\Delta CD4}$  mice fasted for 16 hours (Fast) or gavaged with olive oil (Fat intake) for 2 hours. n=3 or 4 mice per group, representative of two independent experiments. (**I**) Schematic diagram for the IL-22 neutralization experiment in (J). (J) Shown on the left is the distribution of radioactivity in SI segments of F/F and littermate  $A^{\Delta CD4}$  mice after an oral challenge of olive oil containing [ $^3$ H]triolein (18:1) for 2 hours. Mice were treated with 250  $\mu$ g anti-IL-22 ( $\alpha$ IL-22) or control IgG antibody for 16 hours. Shown on the right is the total radioactivity in the SI. n=9 to 11 mice per group, pooled from two independent experiments. For (D), (E), (G, right), and (J, right), data points indicate individual mice; for (G, left) and (J, left), data points indicate mean values. For (D), (E), (G), and (J), data are shown as mean  $\pm$  SEM. For violin plots in (J), lines indicate median and quartiles. The statistical analyses used are as follows: for (D) and (G, right), two-tailed Welsh's test; for (E), ordinary two-way ANOVA; and for (G, left) and (J), two-way ANOVA with Sidak's multiple comparison test. ns, not significant (p>0.05); \*p<0.05; \*\*p<0.05; \*\*p<0.05; \*\*p<0.05; \*\*p<0.05; \*\*p<0.05; \*\*p<0.05;

GRAM domain recruitment to the PM in T cells. The GRAM domain can bind anionic phospholipids other than PS, including phosphatidylinositol 4,5-bisphosphate [PI(4,5)P<sub>2</sub>] and phosphatidic acid, which could serve as alternative PM localization signals in the absence of PS (12, 49). STIM1 is known to reside in PI(4,5)P<sub>2</sub>-rich domains (46, 75, 76), leading us to speculate that Aster-A could be recruited to STIM1 domains by these lipids. Reciprocal PS-PI(4,5)P<sub>2</sub> transport at the PM-ER contact sites has recently been found to fine-tune STIM1 clustering (77, 78). Thus, additional mechanisms of PM phospholipid remodeling may act in conjunction or sequentially with Aster for regulation of TCR signaling and SOCE.

Excess LDL cholesterol can be incorporated into the membranes of immune cells and may promote immunopathology (79–81). In particular, enhanced T<sub>H</sub>17-associated inflammation has been observed in various mouse models of hypercholesterolemia (82–85). Cholesterol internalized by LDL receptor-mediated endocytosis is liberated in the lysosome and then moves back to the PM, where it can be mobilized to the ER by Asters (6, 18, 74). Our results raise the intriguing question of whether Aster-A functions to curtail hypercholesterolemia-induced inflammatory T cell responses by resolving the PM accumulation of LDL-derived cholesterol. Further studies are required to fully understand potential anti-inflammatory roles of Asters in hypercholesterolemia and atherosclerosis.

Finally, our findings show that loss of membrane homeostasis in immune cells affects systemic lipid metabolism. Aster-A expression in T cells is required for appropriate fatty acid absorption and helps determine chronic metabolic responses to HFD. Although we specifically traced the uptake of labeled triolein, which is composed solely of 18:1 fatty acid, diet challenge and fecal analysis suggest a broad impairment of dietary fat absorption in  $A^{\Delta CD4}$  mice. Importantly, increased IL-22 production mediates this T cell-intestinal cross-talk. In line with the well-established role of SFB in inducing IL-22<sup>+</sup> T<sub>H</sub>17 cells (56, 58, 86), Aster-A deficiency led to major changes in IL-22 frequency in the SFB-associated clonal type. These observations imply that Aster-A tunes gut T<sub>H</sub>17 reactivity to commensal bacteria under homeostatic conditions. Our results, along with recent studies demonstrating the metabolic protective role of SFB-elicited T<sub>H</sub>17 cells (62), support the notion that mucosal lymphocytes exert important restraints on intestinal lipid handling.

#### Materials and methods

#### Mice

Aster-A<sup>F/F</sup> (exon 12-16 floxed) and Aster-A<sup>-/-</sup> (global knockout) mice were generated by C57BL/6 ES cell-based gene targeting as described previously (5, 6). Aster-A<sup>F/F</sup> offsprings were backcrossed into C57BL/6N background and crossed with CD4<sup>Cre</sup> (RRID:IMSR\_JAX:022071) line to generate T-cell-specific knockout animals, with Albumin<sup>Cre</sup> (RRID:IMSR\_JAX:003574) line to generate liver-specific knockout animals, with Villin<sup>CreERT2</sup> (RRID:IMSR\_JAX:020282) line to generate tamoxifen-inducible, intestine epithelium-specific knockout animals. For tamoxifen-induced knockout, mice were injected intraperitoneally with 1 mg

tamoxifen in 100 µl corn oil (both from Sigma Aldrich) per day for 5 days and used for experiments 5 days later. All studies involving creflox mice were performed in age- and sex-matched littermates. For studies involving wild-type (CD45.2) mice and congenic (CD45.1) mice, C57BL/6J mice (RRID:IMSR\_JAX:000664) or CD45.1 congenic mice (RRID:IMSR\_JAX:033076) were obtained from The Jackson Laboratories. CD45.1/.2 mice were generated by crossing WT C57BL/6J females with CD45.1 congenic males. IL-22<sup>GFP</sup> mice (RRID:IMSR\_JAX:035005) were purchased from Jax and crossed to  $CD4^{Cre}$ ; Aster- $A^{F/F}$  ( $A^{\Delta CD4}$ ) mice. Il22<sup>hCD4.fl</sup> (Il22<sup>F/F</sup>) mice were originally generated by C. Zindl and C. Weaver (University of Alabama at Birmingham) (87) and were crossed to  $A^{\Delta CD4}$  mice. Unless otherwise specified, 8-14 week old female and male mice were used for in vivo experiments and 6-10 week old female and male mice were used for in vitro experiments. All mice were housed in a temperature-controlled room (22°C with humidity approximately 50-65%) with a 12-hour light-dark cycle (06:00 to 18:00) under specific pathogen-free conditions. Unless otherwise specified in the experimental procedures below, mice were housed in ventilated cages containing nestlets as environmental enrichments, with a maximum of five adult mice per cage. Unless otherwise specified, mice were fed an irradiated chow diet (PicoLab Rodent Diet 20, 5053) and provided water ad libitum. Mice were euthanized by isoflurane overexposure, followed by secondary methods (cervical dislocation or organ harvest). All animal experiments were approved by the UCLA Institutional Animal Care and Research Advisory Committee (Animal protocol B-09-010, R-03-166, R-99-131).

#### Measurement of intestinal fatty acid absorption

For acute fatty acid uptake assay, mice were fasted for 16 hours and then intragastrically gavaged with 5  $\mu$ Ci [ $^{3}$ H]triolein (PerkinElmer) emulsified in 150 µl highly refined, low acidity olive oil (Sigma Aldrich). Blood was sampled using retro-orbital method at 0, 30, 60, 120 min time points. Two hours after gavage, mice were euthanized and small intestine was excised (between the base of the stomach and the cecal junction), flushed with at least 20 ml 0.5 mM sodium taurocholate in PBS, and cut it into 2 cm segments. Segments were incubated with 500 μl of 1N NaOH at 65°C overnight and then mixed with UltimaGold scintillation cocktail (PerkinElmer), and radioactive counts were collected using a Beckman LS6000 scintillation counter. Liver and heart were also harvested and rinsed extensively to remove blood and weighed. Liver medial lobe and heart were incubated with 1 ml and 500 µl of 1N NaOH, respectively, at 65°C overnight and <sup>3</sup>H was counted as above and normalized to tissue weight. Plasma was obtained from blood in K2-EDTA tubes followed by centrifugation at 2,000g for 15 min. Twenty microliters of plasma sample was mixed with 5 ml scintillation cocktail for counting.

#### **Diet studies**

Normal chow diet (PicoLab Rodent Diet 20, 5053) with 13.1 kcal% fat was purchased from LabDiet. The composition of major fatty acids (w/w) are as follows: 46.4% C18:2, 5.6% C18:3, 0.4% C20:4, 8.4%  $\omega$ -3 fatty acids,

Science 9 OCTOBER 2025 12 of 21

15.4% total saturated fatty acids, 20% total monounsaturated fatty acids. Rodent diet with 60 kcal% fat (high-fat diet) was purchased from Research Diet (D12492). The composition of major fatty acids (w/w) are as follows: 34.0% C18:1, 28.7% C18:2, 19.6% C16:0, 10.6% C18:0, 2.0% C18:3, 1.3% C16:1. Mice were co-housed with littermate of both genotypes, single-housed, or grouped by genotype as indicated in individual experimental conditions. Unless otherwise stated, mice were fed indicated diet and given water ad libitum when they reach 8-10 weeks of age or 23 g mean body weight for males, 19 g mean body weight for females. Body composition (fat and lean mass) was measured by magnetic resonance imaging (EchoMRI) at the beginning and end of each study. Body weight was measured weekly. Tissue weights were measured at euthanasia. Food intake measurement, metabolic chamber studies, and fecal 16S sequencing was performed in single-housed male mice.

#### Indirect calorimetry using metabolic cages

Four weeks after high fat diet feeding, respiratory exchange ratios and energy expenditure were measured by indirect calorimetry using the Oxymax Comprehensive Laboratory Animal Monitoring System (Columbus Instruments). Data were analyzed using CalR application (88).

#### Glucose and insulin tolerance assay (GTT/ITT)

Lean mass of mice was determined by MRI on the day prior to GTT/ITT. HFD-fed mice were fasted for 4 hours, followed by intraperitoneal injection of 1 mg per gram of lean mass for glucose, or 2.5 units per kg lean mass for insulin (Humulin) and blood glucose was measured by glucometer (Bayer) at the indicated times.

#### Mixed bone marrow transplant

CD45.1/CD45.2 recipient mice were irradiated using x-ray irradiator with two fractioned doses of 550 cGy with at least 4 hours interval. To harvest bone marrow, femurs and tibias were harvested from F/F,  $A^{\Delta CD4}$ , or competitor CD45.1 mice and removed of muscle tissues. Bone marrow single cell suspension was obtained by homogenizing bones using mortar and pestle. Unfractionated bone marrow cells from donor (CD45.2: F/F or  $A^{\Delta CD4}$ ) and competitor mice (CD45.1) were mixed at 1:1 ratio and 8-10 million mixed bone marrow cells were intravenously injected through the tail vein into the recipients. Recipient mice were given 0.5 mg/ml Baytril (Enrofloxacin) in drinking water for 1-2 weeks prior to transplant and for 2 weeks after transplant to prevent opportunistic infection. Small intestinal lamina propria cells were harvested 8-10 weeks after transplant using the methods described below. Cells were stained with antibodies against CD45.1, CD45.2, CD3, CD4, ALOD4, and RORγt for flow cytometry analysis as described below. All antibody information is reported in table S1.

#### Acute IL-22 treatment and invivo IL-22 neutralization experiments

In vivo IL-22 neutralization was performed by injecting 250  $\mu$ g functional grade anti-human/mouse IL-22 (clone IL22JOP, ThermoFisher) intraperitoneally at the time of fasting (16 hours prior to [³H]triolein gavage). Control mice were injected with 250  $\mu$ g of isotype Rat IgG2a,  $\kappa$  (clone eBR2a). Acute IL-22 treatment was performed by intraperitoneal injection of 1.5  $\mu$ g recombinant mouse IL-22 (Genscript) in DPBS. One hour later, mice were used for fatty acid absorption assay.

#### Depletion of microbiota by broad-spectrum antibiotics

Caging and food were sterilized by autoclaving/irradiation. Mice were given broad spectrum antibiotics (1 g/liter Ampicillin, 1 g/liter Neomycin, 1 g/liter Metronidazole, 0.5 g/liter Vancomycin, 1 g/liter Gentamycin, and 0.01 g/liter amphotericin B) in sterile drinking water for 2 weeks. Feces before and after antibiotics treatment were collected. Bacterial DNA was isolated from same quantity of feces using Quick-DNA Fecal/Soil Microbe Miniprep Kit (Zymo Research). Quantitative PCR of 16s rRNA was performed using primers in table S2.

#### Intraperitoneal anti-CD3 $\epsilon$ antibody

Twenty micrograms of anti-mouse CD3 $\epsilon$  (clone 145-2C11) or control polyclonal Armenian hamster IgG (both from BioXCell) was diluted in DPBS and injected peritoneally to mouse at indicated times prior to sacrifice. For ALOD4 staining, mesenteric lymph nodes were resected and processed to single cell suspension on ice in DPBS (Ca<sup>2+</sup>, Mg<sup>2+</sup>). Cells were stained with ALOD4 and live/dead stain for 1 hour at 4°C, followed by fixation and permeabilization (eBioscience FOXP3 Transcription Factor staining set), and antibody staining as described below.

#### **Plasmids**

Table S3 lists plasmids used and generated by this study. Full length mouse Aster-A coding sequence was cloned into: (i) 3xHA-TurboID pRetrox with TurboID (Addgene Plasmid #155203) located at N terminus of Aster-A GRAM domain with a GGGGS linker; (ii) MSCV-IRES-hCD2 (Addgene Plasmid no. 133061) vector with an N-terminal HA tag and GGGGS linker; (iii) an inframe N-terminal mCherry and 3x GGGGS linker, all by Gibson assembly (NEB). Aster-A functional mutations were identified from homologous amino acids between mouse Aster-A and human/mouse Aster-B (19, 49) and cloned into MSCV-IRES-hCD2 vector by site-directed mutagenesis. C-terminal Myc-GGGGS-tagged mouse STIM1 was cloned from pcDNA3.1 mSTIM1 myc (Addgene Plasmid no. 17732) and inserted into pMSCV-Blast (Addgene Plasmid no. 75085) vector by Gibson assembly. Full-length human Aster-A was cloned from Jurkat cDNA and mCherry was tagged at N-terminal using methods above into a pMSCV-hygro (Addgene Plasmid no. 34565) vector. For CRISPR plasmids, guide RNA sequences (described below) were cloned into pSCAR\_sgRNA\_puro-mKate-lox2272 (Addgene Plasmid no. 162076) or pSCAR\_sgRNA\_hygro-tagBFP-lox5171 (Addgene Plasmid no. 162070) vectors using BsmBI sites.

#### Viral production and transduction

For retrovirus production for murine cells, 2.5 µg transfer plasmid and 0.63 µg pCL-ECO were co-transfected to  $1 \times 10^6$  Platinum-E cell line in 6-well plate using OptiMEM and FugeneHD reagent for 6-8 hours. Media was replaced with appropriate culture media for the target cell, and virus supernatant was harvested at 48 and 72 hours post transfection. For retrovirus production for human cells, 2.5 µg transfer plasmid was transfected to Phoenix-AMPHO cell line and virus was harvested at 48 hours. For lentivirus production, 2.5 µg transfer vector, 1.875 µg psPAX2, 1.25 µg pMD2.G was co-transfected to Lenti-X cell line in a similar procedure as above. For integration deficient Cre lentivirus, 2.5 μg pLX-Cre-ppl-del, 1.875 μg psPAX2 D64V, 1.25 μg pMD2.G was co-transfected to Lenti-X cell line. For viral transduction of suspension cell lines, viral supernatant was harvested and cleaned through a 0.45 µm filter. Cells were spin infected in 12-well plates with 1-2 ml viral supernatant containing 8 µg/ml polybrene (for cell lines) or 10 µg/ml Protamine Sulfate (for primary T cells). Viral supernatant was replaced with normal growth medium 4-6 hours later and antibiotics selection was performed 48-72 hours post transduction. For some experiments, transduction was repeated 24 hours later to increase efficiency.

# Cell lines, construction of stable overexpression cells, and CRISPR knockout cells

Platinum-E (RRID:CVCL\_B488) retroviral packaging cell line was obtained from Cell Biolabs. Lenti-X 293T cell line (RRID:CVCL\_4401) was obtained from Takara Bio. Phoenix-AMPHO (RRID:CVCL\_H716), EL-4 (RRID:CVCL\_0255), Jurkat (RRID:CVCL\_0065) cell lines were obtained from the American Type Culture Collection.

To construct stable TurboID-expressing EL-4 lines, EL-4 cells were transduced with retrovirus containing pRetroX-3xHA-TurboID or pRetroX-3xHA-TurboID-GGGGS-mAster-A. Cells were selected with 10  $\mu$ g/ml puromycin for 1 week and maintained in 0.3  $\mu$ g/ml puromycin. To construct stable mCherry-tagged mAster-A expressing EL-4 line,

Science 9 OCTOBER 2025 13 of 21

#### **RESEARCH ARTICLE**

EL-4 cells were transduced with retrovirus containing pMSCV-mCherry-GGGGS-mAster-A, mCherry positive cells were FACS-sorted and used without further subcloning. To construct stable HA-tagged mAster-A expressing EL-4 line, EL-4 cells were transduced with retroviruscontaining pMSCV-HA-GGGGS-mAster-A (WT or R186W mutant)-IRES-hCD2, cells were FACS-sorted by surface hCD2 expression. STIM1 was further introduced by infecting HA-Aster-A cell lines with virus containing pMSCV-STIM1-Myc-His-Blast and cells were selected with 10  $\mu$ g/ml Blasticidin for >1 week and maintained on 1  $\mu$ g/ml Blasticidin. To construct PM-RA and B-GRAM-H (B-GRAM-H-ddFP) expressing cell lines, EL-4 or Jurkat cells were transduced with lentivirus containing pLJM1-PM-RA-BlastR and pLJM1-B-GRAM-H-NeoR. Cells were selected with 2 mg/ml G418 and 50  $\mu$ g/ml Blasticidin for 1 week and maintained in 0.5 mg/ml G418 and 10 µg/ml Blasticidin. Protein expression in overexpression or reconstitution experiments was confirmed by Western blot.

To construct Aster-A knockout Jurkat human T cell lines, pSCAR-Cas9-GFP was introduced by lentiviral transduction and stable polyclonal Cas9-GFP expressing Jurkat cells were selected by FACS sorting. Cas9-GFP Jurkat cells were co-transduced with pSCAR\_sgRNA1\_puro-mKate-lox2272 or pSCAR\_sgRNA2\_hygro-tagBFP-lox5171 virus with two distinct gRNAs: gRNA1 targeting hAster-A exon 10 (5'-GTCTGTCAATAGCTCCTCAC-3') and gRNA2 targeting exon 14 (5'-TCTCAATGAGCGACTTCACC-3'). The resultant deletion of exons in between will eliminate the majority of ASTER domain in addition to a frame shift. As control, Cas9-GFP Jurkat cells were transduced with the above sgRNA vector containing viruses where sgRNA1 (5'-GCACTACCAGAGCTAACTCA-3') and sgRNA2 (5'-GTGCGAATACGCCACGCGAT-3') do not target any human genome sequence. Cells were selected with 50 µg/ml Blasticidin, 10 µg/ml Puromycin, and 500 μg/ml Hygromycin for 1 week to allow deletion. Jurkat cells were single-cloned by FACS, and GRAMD1A knockout clones were selected by PCR and subsequently confirmed by the absence of hAster-A protein by Western blotting (anti-hAster-A, Bethyl labs). Control clone was selected to match growth rate, morphology, and cell size of the KO clone. Subsequently, Cas9-GFP, mKate, and tBFP was removed by transducing single clones with integrase deficient virus and isolated by GFP/mKate/tBFP-triple negative FACS sorting. hAster-A KO Jurkat clones were further reconstituted with HA-tagged hAster-A, or HA alone empty vector (EV) using amphotropic retrovirus and were selected by 500 µg/ml Hygromycin for 2 weeks.

#### Plasma and tissue lipid quantification

Plasma lipids were measured by colorimetric assay with L-Type TG M kit (Wako). Tissues were homogenized by dounce homogenizer in JP lysis buffer [10 mM Tris-HCl pH 7.4, 150 mM NaCl, 1 mM EDTA, Halt protease inhibitor cocktail (ThermoFisher)] and Folch method was used to extract lipids from materials containing 0.5-1 mg tissue protein (89). Protein content was measured by Bicinchoninic Acid Assay Protein Assay Kit (Pierce). Extracted lipids were dried under inert gas and resuspended in isopropanol and quantification was performed using the previously described kits. For cholesterol measurement in culture media, 1 ml of media was used for lipid isolation and quantification using Total Cholesterol E Kit (Wako).

#### Measurement of fecal NEFA and lipid species

Littermate mice were fed with high fat diet for 10 days and then single-housed with fresh cellulose bedding. Feces accumulated for 48 hours were collected, snap frozen, and pulverized using mortar and pestle. One hundred milligrams of fecal homogenate was used for lipid extraction with 19 volumes of 2:1 (v/v) chloroform:methanol using the Folch method. Solvent was removed by drying under nitrogen gas, resuspending in isopropanol, and measured using NEFA-Hr kit (Wako).

Thin layer chromatography was performed using lipid extraction from 25 mg fecal homogenates. Fecal lipids were extracted as described above, resuspended in chloroform, and dotted on a Silica Gel 60 TLC plate (Millipore Sigma). Samples are stacked using solvent 1 system (CHCl $_3$ /MeOH = 2:1) and neutral lipid species were subsequently separated using solvent 2 system (Heptane/Isopropyl Ether/glacial Acetic Acid = 15:10:1). A mixed lipid standard (mouse liver lipid extract supplemented with 20 mM 18:1 fatty acid) was run along the samples to identify triglycerides and free fatty acids. Separated lipids were visualized by exposing to iodine vapor for 30 min.

#### Protein isolation from the intestinal epithelium

Intestines were harvested immediately following euthanasia and extensively flushed with PBS containing 1 mM dithiothreitol (DTT), Halt phosphatase and protease inhibitor cocktail. The proximal 1/6 of the intestine was designated as duodenum, middle 3/6 as jejunum, and last 2/6 as ileum. Indicated intestinal section was excised and longitudinally opened to expose the lumen. Epithelial scrapings were obtained by gently scraping the luminal tissue with two glass slides. To prevent protein degradation, scrapings were immediately snap frozen in liquid nitrogen. Scrapings were cut and weighed on dry ice, and approximately 100 mg sample was resuspended in 1 ml DS buffer [150 mM NaCl, 1.5 mM DTT, 50 mM Tris HCl pH 7.4, 1.25 mM EDTA, Halt phosphatase and protease inhibitor cocktails, 1 mM phenylmethylsulfonyl fluoride (PMSF)] and immediately homogenized on ice using motorized Dounce (850 rpm, 15 strokes). Homogenates were further sonicated (3 s  $\times$  3 at 50%) and lysates were cleared (2000g, 10 min, 4°C).

#### **Total cell protein lysate**

Cells were washed with PBS by centrifugation for at least 3 times, and pellet was lysed with RIPA buffer (containing protease and phosphatase inhibitor cocktails) on ice for 30 min. Lysate was cleared by centrifugation at 12,000 xg for 15 min. In some experiments, boiled 2X LDS sample buffer was directly added to cell pellets and DNA was sheared by sonication.

#### Western blot analysis

Protein content was determined by the Bicinchoninic Acid Assay Protein Assay Kit (Pierce) or Pierce 660 kit. An equal amount of protein was loaded into the NuPAGE 4-12% Bis-Tris gels (Invitrogen). Proteins were transferred to PVDF blotting membrane (Amersham Hybond). Membranes were blocked for 1 hour at room temperature with 5% non-fat milk in TBST buffer (TBS + 0.1% Tween 20) and incubated with primary antibodies listed in table S1 in 5% non-fat milk or 5% bovine serum albumin (BSA). IR800-, Cy3-, Cy5-, Horseradish peroxidase-conjugated anti-mouse, anti-rat and anti-rabbit IgG were used as secondary antibodies. The blot membrane was visualized using the Immobilon Forte Western HRP Substrate, SuperSignal West Femto Maximum Sensitivity Substrate, or directly imaged for fluorescent signal using ChemiDoc MP (BioRad).

#### RNA extraction and gene expression analyses

For tissue RNA isolation, approximately 50-100 mg frozen tissue was immediately homogenized in Trizol Reagent using preloaded 4 mm metal beads and Qiagen Tissue Lyzer. For RNA isolation from cells, cells pellets were lysed with 0.5-1 ml TriZol reagent for 5 min. Total RNA was extracted using the TRIzol method, quantified by NanoDrop (ThermoFisher) and reverse transcribed. cDNA was quantified by real-time PCR using iTaq Universal SYBR Green Supermix (Bio-Rad) on a QuantStudio 6 Flex 384-well qPCR system (Applied Biosystems). Gene expression levels were determined by using  $\Delta\Delta$ Ct method. Housekeeping gene 36b4 was used for normalization and every sample was analyzed in triplicate. Primers used for real-time PCR are listed in table S2.

#### Purification and fluorophore conjugation of ALOD4 and OlyA

pALOD4, pALOD4 non-binding mutant (G501A/T502A/T503A/L504A/Y505A/P506A) and pOlyA plasmids were obtained from AddGene or

Science 9 OCTOBER 2025 14 of 21

gifted from the Radhakrishnan lab (table S3) and proteins were purified according to a previously published method (4). Briefly, plasmids encoding specified proteins were expressed in BL21 (DE3) pLysS Escherichia coli (Invitrogen). Cell pellets were lysed by sonication in lysis buffer containing 50 mM NaH<sub>2</sub>PO<sub>4</sub>, pH 7.0, 300 mM NaCl, 1 mg/ml lysozyme, 1 mM DTT, 2 mM PMSF and Halt protease inhibitor cocktail. The protein was bound to HisPur Ni-NTA Agarose resin (Thermo Scientific), washed twice with 50 mM imidazole, eluted with 300 mM imidazole, and subjected to size exclusion chromatography on Superdex 200. Fractions containing specified protein were concentrated to 1 mg/ml and stored at -80°C with glycerol until use. For ALOD4 labeling, ALOD4 was conjugated to Alexa Fluor 555-maleimide, Alexa Fluor-488-maleimide (ThermoFisher), or ATTO647N-maleimide (SigmaAldrich) followed by affinity purification using HisPur Ni-NTA Agarose resin and dialyzation. Labeling efficiency was determined using on Nanodrop (Thermo Fisher).

#### **ALOD4 and OlyA staining**

For confocal imaging, cells were plated on Shi-Fix coverslips or poly-D-lysine coated coverslips. Cells were washed with DPBS ( $Ca^{2+}$ ,  $Mg^{2+}$ ) with 0.2% BSA three times. The ALOD4 working solution (20 µg/ml in DPBS + 0.2% BSA) was passed through a 0.45 µm filter before addition to cells and incubating while rotating at 4 °C in the dark for 1-2 hours. Coverslips were washed three times with cold DPBS before being fixed with 3% paraformaldehyde (PFA) for 10-15 min at room temperature. After fixation, slides were washed with DPBS three times. For unconjugated ALOD4, cells were incubated with an anti-His antibody (27E8) overnight before incubation with fluorescently labeled secondary antibodies for 1 hour at room temperature. Cells were mounted on slides with ProLong Diamond Antifade Mountant with DAPI (Invitrogen). Images were acquired using an Inverted Leica TCS-SP8-SMD Confocal Microscope.

For flow cytometry of ALOD4 staining, cells were washed with cold DPBS ( $Ca^{2+}$ ,  $Mg^{2+}$ ) three times. Cells were incubated with ALOD4 working solution ( $20~\mu g/ml$  in DPBS) and Fixable Viability Dye eFluor450 (eBioscience) while rotating at 4°C in the dark for 1-2 hours. Cells were washed three times with DPBS containing 0.2% fatty acid-free BSA and fixed for 10-15 min with Fix/Perm buffer (BD) at 4°C before proceeding to the remaining flow cytometry staining procedure. For flow cytometry analysis of plasma membrane ALOD4 following anti-CD3 $\epsilon$  mediated activation, plasma membrane accessible cholesterol density was estimated by normalizing ALOD4-ATT0647N signal to forward scatter (FSC) parameter to regress out the increased cell size and surface area using the following conversion formula:

PM accessible cholesterol density = Intensity < ATTO647N >/  $\left[4\pi(Intensity < FSC >)^2\right]$ 

For Western blot analysis, cells were washed extensively with DPBS  $(Ca^{2+}, Mg^{2+})$ . Equal numbers of cells were incubated with ALOD4 and OlyA working solution (both 20  $\mu$ g/ml) as above. Surface ALOD4/OlyA-bound cells were lysed with RIPA buffer before being probed with anti-His (27E8).

#### Histology

Whole mouse tissue was fixed in neutral formalin solution for at least 48 hours at room temperature, then rinsed extensively with water and preserved in 70% ethanol. Tissues were paraffin-embedded and cross-sectioned at 5  $\mu m$  thickness. Hematoxylin and eosin (H&E) staining was performed by UCLA Translational Pathology Core Laboratory using routine procedures.

#### Immunofluorescence of the small intestine

Mice were fasted for 16 hours to synchronize metabolic status, then were intragastrically gavaged with 150  $\mu$ l refined low acidity olive oil.

Two hours later, mice were euthanized and cardiac perfused with 10 ml cold DPBS. Small intestine was excised between stomach to cecum and flushed with 10-15 ml cold DPBS to remove luminal content, followed by a slow luminal flush of 10 mL 4% paraformaldehyde to flashfix the luminal epithelium. Small intestine was then longitudinally opened and rolled into a Swiss roll with luminal facing out, immobilized in tissue cassette and fixed overnight in 4% PFA on a 4°C rocker. Tissues were then dehydrated in 20% Sucrose in PBS for 24-48 hours on a 4°C rocker before embedding in OCT. Embedded tissue were sectioned at 18 µm thickness and attached to Superfrost Plus slides and further fixed with pre-chilled methanol in -20°C for 20 min, airdried and rehydrated with PBST (PBS containing 0.05% Tween-20). Slides were incubated in blocking/permeabilization buffer [PBS + 0.3% Triton X-100 + 10% normal goat serum block (BioLegend)] for 1-2 hours at room temperature and stained overnight in blocking/permeabilization buffer containing anti-EPCAM-AlexaFluor 488 (G8.8). Slides were washed three to five times with PBST, stained with DAPI and lipidTOX-Red for 1 hour at room temperature, and mounted with Prolonged Diamond anti-fade mounting reagent (all from ThermoFisher). For confocal imaging of the Swiss roll for lipid droplet quantification, tile scan images were acquired on a Zeiss LSM900 confocal microscope using Plan-Apochromat 10x/0.45 M27 and 30 µm Z-stack to capture the full thickness of the tissue sections. Following acquisition, the tile scan images were processed using stitch feature and then displayed as a maximum intensity projection.

#### Quantification of lipid droplets

To quantify lipid droplet size and number from enterocytes in the intestine confocal images, stitched maximum intensity projection images were deconvoluted in ImageJ with the DeconvolutionLab2 plugin using a theoretical PSF generated with the PSFGenerator plugin. Processed images were then loaded into CellProfiler (90) for lipid droplet quantification using a customized pipeline. Briefly, EPCAM signal was used to delineate cell membranes and mask lumenal artifacts. LipidTOX-stained lipid droplets were identified using the *IdentifyPrimaryObjects* module and measurements extracted with the *MeasureSizeShape* module. Droplet measurements were inspected and analyzed in R.

#### Live-cell confocal imaging

First,  $0.25 \times 10^6$  mCherry-Aster-A expressing EL-4 cells were resuspended in 500 µl warm Ringer's solution (155 mM NaCl, 4.5 mM KCl, 2 mM CaCl<sub>2</sub>, 1 mM MgCl<sub>2</sub>, 10 mM D-glucose, 5 mM HEPES) and plated onto poly-D-lysine coated 35 mm No. 1.5 Glass Coverslip culture dish (MatTek). Cells were then stained with AlexaFluor 647 anti-TCRβ (nonblocking clone H57-597, 2.5 µg) for 30 min on ice. Confocal live cell imaging was performed using the Leica Confocal SP8-STED/FLIM/ FCS microscope equipped with an environmental control stage (5% CO<sub>2</sub>, 37°C chamber and objective) and the 100x/1.40 objective. Live images  $(2048 \times 2048 \text{ pixels per frame})$  were collected at 8000-Hz bidirectional scan speed with the resonance scanner using the following parameters: frame sequential mode, 15 s interval per acquisition, Pinhole = 1 Airy Unit (580 nm emission), pixel size = 102.8 pixels per micron with 5.84xdigital zoom. mCherry channel was excited at 587 nm with 15% laser power and collected with a PMT gain of 1000V and a band pass of 595 to 640 nm. AlexaFluor647 channel was excited at 653 nm with 20% laser power and collected with a HyD gain of 200% and a band pass of 660 to 779 nm. Deconvolution was performed using the Leica LAS X Lightning Deconvolution module using the "adaptive" strategy. Bleach correction was performed using Histogram Matching Method (FIJI/ImageJ).

# Dimerization-dependent fluorescent protein-fused GRAM domain recruitment assay

B-GRAM-H-ddFP expressing Jurkat cells were resuspended in Ringer's solution and warmed up to  $37^{\circ}\text{C}$  for 10-15 min. Live single cells were

Science 9 OCTOBER 2025 15 of 21

gated based on forward and side scatter parameters. ddFP signals were recorded using mCherry channel (Ex-561 nm/ Filter-585/15) on a BD LSR Fortessa flow cytometer. For TCR stimulation, 5 µg/ml anti-human CD3 was added for 15 min and then 2 min of baseline signal was acquired before addition of 10 µg/ml streptavidin (crosslinking agent, BioLegend) and recording for another 5-10 min. Following first segment of acquisition, cells were returned to 37°C and were subsequently recorded at t = 15, 30, 60 min post activation (for 1 min each) to obtain kinetics over a longer time frame. For ionomycin stimulation, 1 µM ionomycin was directly added following the 2-min baseline recording. To pharmacologically inhibit phosphatidylserine scramblase TMEM16F, cells were pre-incubated with 10 µM 1PBC (Sigma Aldrich) for 30 min prior to recording. Kinetics platform in FlowJo v10 was used to generate kinetics curve.

#### **Electron microscopy**

Ten-week-old F/F and  $A^{\Delta CD4}$  female mice were fasted for 16 hours, then refed with refined low acidity olive oil for 2 hours. Small intestine were harvested, contents were flushed with PBS and a 0.5 cm ring shaped segment from proximal jejunum (measured at 8-10 cm from the end of stomach) was harvested and directly placed into EM fixative (2.5% glutaraldehyde, 2% paraformaldehyde, 2.1% sucrose 0.1 M sodium cacodylate) at 4°C overnight. The following day, the samples were washed 5 min, 5 times in cold 0.1 M sodium cacodylate and then postfixed with reduced osmium (2% OsO<sub>4</sub>, 1.5% potassium ferricyanide, 0.1 M sodium cacodylate) for 1 hour. Next, samples were washed 5 times, 5 min each in cold H<sub>2</sub>O then treated with 1% thiocarbohydrazide for 20 min at room temperature. Samples were then rinsed with H<sub>2</sub>O for 5 times, 5 min each, and stained again with osmium (2%OsO4 in H2O) for 30 min. After another round of H2O washes, the tissue was stained with 1% uranyl acetate (SPI Chem) at 4°C overnight. Tissues were dehydrated by incubating in a graded series of ethanol solutions (30%, 50%, 70%, 85%, 95%, 100%, 3 times each) for 8 min each. Then tissues were infiltrated with 33% (in acetone) EMbed 812 for 1 hour, 66% overnight, then 100% for 4 hours. Individual tissue pieces were then embedded in a flat mold and polymerized in a vacuum oven for 48 hours. Resin blocks were then trimmed and 500 nm sections were collected onto small silicon wafers using a Leica UC6 ultramicrotome and a Diatome diamond knife. For backscattered electron microscopy (BSEM): Wafers were mounted onto SEM stubs with double-sided carbon tape and imaged using a Zeiss Supra 40VP SEM equipped with a backscattered electron detector. Accelerating voltage was set to 13KeV and working distance at approximately 5 mm. BSEM was performed at the Electron Imaging Center for Nanomachines which is a part of the California NanoSystems Institute at UCLA.

#### Tissue processing and immune cell isolation

For isolation of immune cells from lymphoid tissues (spleen, lymph nodes, thymus), tissues were homogenized between two frosted slides. Single cell suspension was obtained by filtering using a 70  $\mu$ m strainer. In some experiments, red blood cell removal was performed using Hybri-Max Red Blood Cell Lysing Buffer (Sigma Aldrich).

For isolation of immune cells from small intestine lamina propria, tissues were carefully removed of mesenteric fat and Peyer's patches. Then intestinal tissues were flushed of luminal contents, cut longitudinally open, and excised into 1-inch pieces. Cleaned tissues were extensively washed in cold HBSS buffer (HBSS + 25 mM HEPES) and then incubated in DTT buffer (HPSS + 25 mM HEPES + 3% fetal bovine serum + 1 mM DTT) for 10 min in an orbital shaker (200 rpm) at 37°C, extensively vortexed, and mucus in supernatant was removed through a 100  $\mu$ m strainer. Epithelial layer was removed by two rounds of incubation with EDTA buffer (HBSS + 25 mM HEPES + 3% fetal bovine serum + 5 mM EDTA) for 10 min in an orbital shaker (200 rpm) at 37°C and followed by passing through 100  $\mu$ m strainer. Remaining

tissue was washed in HBSS, finely minced and digested (RPMI-1640, 0.5% fatty-acid free BSA, penicillin/streptomycin, glutamine, 1 mg/ml Collagenase D and 100 µg/ml DNase-I, 100 µg/ml Dispase II) for 35-55 min in an orbital shaker (150 rpm) at 37°C. Tissues were then vigorously vortexed and RPMI-1640 media containing 10% FCS was added. The digested tissue was filtered using 40 µm strainer. Cells were pelleted and loaded on 40%/80% Percoll gradient centrifugation (1,000g, 20 min at room temperature with no deceleration). Lamina propria mononuclear cells were collected from the interphase and washed with cold culture media or FACS buffer. For ALOD4 staining of ex vivo lamina propria cells, tissues were isolated and digested in 0.5% fatty-acid free BSA (Sigma) containing buffer in replacement of FCS.

For isolating adipose stromal-vascular fraction (SVF), mice were perfused with 10 ml cold PBS and adipose tissues were excised and weighed. Tissues were minced into 1 mm cubes and incubated in digestion buffer (HBSS + 10 mM HEPES + 10 mg/ml Collagenase D + 2% FCS + 10 mM CaCl $_2$ , 4 ml/g tissue) for 40 min with orbital shaking (100 rpm) at  $37^{\circ}\text{C}$ . Digested tissue was vortexed for 2 min, pushed through 70  $\mu\text{m}$  strainer and pelleted (500g, 10 min). Supernatant containing mature fat cells were discarded and pellet containing SVF cells was washed again with cold culture media or FACS buffer.

#### Flow cytometry staining and analysis

Antibodies used for flow cytometry analysis are listed in table S1. For the surface flow cytometry analysis, cell suspensions were resuspended in FACS buffer (DPBS, 2% FCS or 0.5% BSA, 2 mM EDTA), blocked with Fc block (anti-CD16/CD32), and subsequently stained with fluorophore conjugated antibodies. In some experiments, biotin-conjugated surface antibodies were used and subsequently stained with secondary streptavidin-PerCP-Cy5.5 (Biolegend). For non-conjugated ALOD4, a secondary PE anti-His Tag antibody (J095G46) was used and sample stained with secondary antibody but not ALOD4 was used as negative control. DAPI or LIVE/DEAD Fixable dyes were used to exclude dead cells. For intracellular cytokine staining, cells were cultured in 50 ng/ ml PMA (Sigma-Aldrich), 1 µM ionomycin (Sigma-Aldrich) in the presence of 5  $\mu$ g/ml brefeldin A (BioLegend) for 4-6 hours and then were stained with Live/Dead Fixable dye according to manufacturer's protocol. Cells were fixed and permeabilized using the Cytofix/Cytoperm kit (BD) and stained with antibodies diluted in permeabilization buffer. For intracellular transcription factor staining, cells were stained with Live/Dead Fixable dye and then fix, permeabilized according to FOXP3 fix/perm buffer set (eBioscience) protocol. Samples were acquired on a BD Verse or LSR-II flow cytometer. Data were analyzed using FlowJo v10. Unless specifically indicated, cells are identified based on Forward and Side Scatter (FSC/SSC) and single cells are gated using FSC-A/H/W and SSC-A/H/W parameters. Experiment-specific flow gating strategies are shown in supplemental figures.

#### T cell isolation and differentiation

Naïve CD4 T cells were isolated from spleen and peripheral lymph nodes of 6-12 week old mice using naïve CD4 T cell isolation kit (Miltenyi or BioLegend). For "pathogenic" T<sub>H</sub>17 (pT<sub>H</sub>17) differentiation, naïve CD4 T cells were activated using plate-bound anti-CD3/ CD28 (5 µg/ml) in X-VIVO15 media (LONZA) containing 25 ng/ml mIL-6 (Peprotech), 5 ng/ml hTGFβ1 (Miltenyi), 20 ng/ml mIL-1β (Peprotech), 20 ng/ml IL-23 (R&D Systems), 10 μg/ml anti-IFNγ, and 10 μg anti-IL-4 (both from Biolegend) for 4 days. For restimulation experiments, day-4 pT<sub>H</sub>17 cells were removed from differentiation cocktail, washed and rested in fresh X-VIVO media overnight. T<sub>H</sub>17 cells were restimulated using 1-2 µg/ml plate-bound anti-CD3/CD28. Differentiation of other T-cell subtypes was performed as follows: Th0: 20 unit/ml IL-2 (BioLegend); Th1: 20 unit/ml IL-2, 10 ng/ml IL-12 (Peprotech), 10 μg/ml anti-IL-4; Th2: 20 unit/ml IL-2, 5 ng/ml IL-4 (Peprotech), 10 μg/ml anti-IFNγ; non-pathogenic T<sub>H</sub>17: 25 ng/ml mIL-6, 5 ng/ml hTGF $\beta$ 1, 10 µg/ml anti-IFN $\gamma$ , and 10 µg anti-IL-4; Th22: 25 ng/ml

Science 9 OCTOBER 2025 16 of 21

mIL-6, 20 ng/ml mIL-1 $\beta$ , 20 ng/ml IL-23, 400 nM FICZ (Invivogen), 10  $\mu$ g/ml anti-IFN $\gamma$ , and 10  $\mu$ g/ml anti-IL-4; Treg: 50 unit/ml IL-2, 5 ng/ml hTGF $\beta$ 1, 10  $\mu$ g/ml anti-IFN $\gamma$ , and 10  $\mu$ g/ml anti-IL-4.

#### Retroviral transduction of primary T<sub>H</sub>17 cells

Naïve CD4 T cells were activated by plate-bound anti-CD3/CD28 (5  $\mu g/ml)$  in differentiation X-VIVO15 media containing 25 ng/ml mIL-6, 5 ng/ml hTGF $\beta$ 1, 20 ng/ml mIL-1 $\beta$ , 20 ng/ml IL-23, 10  $\mu g/ml$  anti-IFN $\gamma$ , and 10  $\mu g/ml$  anti-IL-4 for 24 hours. Activated cells were then spin infected (2,500 rpm, 90 min, 32°C) with retroviral supernatant containing 20 units/ml IL-2 and 10  $\mu g/ml$  protamine sulfate (Sigma-Aldrich), and incubated with viral supernatant for additional 4-6 hours. Then cells were returned to differentiation media. Spin-infection was repeated 24 hours later. Successfully transduced T cells were identified by their surface expression of human CD2, which does not cross-activate mouse TCR.

#### TCR nanocluster and monomer purification

Membrane fraction was purified from primary T<sub>H</sub>17 cells using a modified serial lysis method (39). First, 5-10  $\times$  10<sup>6</sup> T cells were extensively washed in cold PBS, incubated in hypotonic lysis buffer (10 mM HEPES, 42 mM KCl, 5 mM MgCl<sub>2</sub>, protease inhibitor cocktail, 1 mM PMSF), and mechanically disrupted using tight-fitting glass Dounce homogenizer. Whole cells and nuclei were removed by centrifugation for 10 min at 150g. Membrane patch was purified by ultra-centrifugation at 100,000g for 30 min at 4°C and pellet was washed once more with hypotonic lysis buffer. To extract TCR nanocluster, membrane pellet was resuspended in serial lysis buffer (20 mM Tris-Cl pH 8, 2 mM EDTA, 137 mM NaCl, 10%v/v glycerol, protease inhibitor cocktail, 1 mM PMSF) containing 1% saponin and rotated end-to-end at 4°C for 15 min, followed by centrifugation at 14,000g for 15 min to obtain supernatant. The insoluble pellet was again resuspended in 1% saponin serial lysis buffer for a total of three rounds of extraction and supernatant was pooled. To extract TCR monomer, the insoluble pellet from previous step was further extracted for three rounds in serial lysis buffer containing 0.5% Brij97. Pooled extracts were reduced in LDS sample buffer and blotted with anti-CD3ζ.

#### Flow cytometry-based Ca<sup>2+</sup> flux assay

Isolated naïve CD4 T cells were cultured in X-VIVO15 media overnight before performing the  $Ca^{2+}$  flux assay. Differentiated  $T_{\rm H}$ 17 cells were removed from differentiation cocktail, washed and "rested" overnight in fresh X-VIVO15 media without further stimulation or IL-2. For flow cytometry-based assay, T cells were labeled with 1 µM Fluo-4-AM and 1 μM FuraRed-AM mixed 1:1 with 20% Pluronic F-127 in DMSO (all from ThermoFisher) in X-VIVO15 media for 30 min at room temperature with gentle rotation, and then washed and resuspended in Ringer's solution. Labeled cells were warmed up to 37°C for 10-15 min to allow cleavage of AM ester and were kept in 37°C water bath during recording. Live single cells were gated based on forward and side scatter parameters. Fluo-4 (Ca<sup>2+</sup> bound) and FuraRed (Ca<sup>2+</sup> unbound) fluorescence were recorded on Ex-488nm/ Filter-530/30 and Ex-488nm/ Filter-695/40 channel on the following sequence: (i) 3 min of baseline acquisition; (ii) 15 min following the addition of 5 μg/ml of biotin-anti-CD3ε and biotin-anti-CD28 for mouse T cells, or 5 µg/ml of biotin-anti-hCD3 for Jurkat cells; (iii) 15 min following the addition of 10 μg/ml streptavidin, (iv) 5 min following addition of 1 μM Ionomycin (Sigma-Aldrich). Kinetics platform in FlowJo v10 was used to plot time versus median Fluo-4/FuraRed ratio and to calculate peak value and area under curve.

#### Single-cell ratiometric Ca<sup>2+</sup> imaging

Single-cell  $\text{Ca}^{2+}$  flux assay for T cells was modified from a previous publication (52). Overnight rested T cells were loaded at  $1\times 10^6$  cells per ml with 1  $\mu$ M Fura 2-AM for 30 minutes at 25°C, resuspended in loading medium, and attached to poly-L-lysine-coated coverslips for 15 min.

For  $[Ca^{2+}]_i$  measurements, cells were mounted in a RC-20 closed bath flow chamber (Warner Instrument Corp., Hamden, CT) and analyzed on an Olympus IX51 epifluorescence microscope with Slidebook (Intelligent Imaging Innovations, Inc.) imaging software. Fura-2 emission was detected at 510 nm with excitation at 340 and 380 nm, and the Fura-2 emission ratio (340/380) was acquired at every 5-s interval after subtraction of background. For each experiment, at least 100 individual cells were analyzed using OriginPro (Originlab).

#### Biotin affinity purification and sample preparation for proximity labeling

EL-4 lines stably transduced with pRetroX-3xHA-TurboID-Aster-A or pRetroX-3HA-TurboID (empty vector) were constructed as described above. Tight TRE promoter has a leakage expression in EL-4 cell line, which resulted in moderate expression of 3x-HA-TurboID-Aster-A and stable cell lines were therefore used without doxycycline induction.

TurboID or TurboID-Aster-A expressing EL-4 cells were cultured in 10% FCS complete culture media or starved with a cholesterol-depletion media containing 1% Lipoprotein-deficient serum, 5  $\mu M$  Simvastatin, 50 μM Mevalonate for 18-24 hours. Depleted cells were either loaded with 100 μM MβCD-Cholesterol or maintained in fresh cholesteroldepletion media for 1 hour and 15 min. Cholesterol-rich samples were maintained in 10% FCS complete media for the same time. Then, 50 µM Biotin was added to the culture media for the last 30 min to facilitate labeling. Isolation of biotinylated proteins were performed based on a modified protocol (41). Cells were collected and washed extensively with cold PBS and incubated with lysis buffer (RIPA buffer containing 1X Halt protease and phosphatase inhibitor and 1 mM PMSF) with gentle agitation for 30 min on ice. Lysate were cleared by centrifugation at 12,000g for 15 min and protein concentration was determined by BCA assay. Equal quantities (900 µg) of cleared lysates in lysis buffer were incubated with 75 μl Streptavidin magnetic beads (Thermo Fisher Pierce) overnight at 4°C with gentle rotation. The beads were then washed at room temperature twice in lysis buffer for 5 min each, once with 1 ml 1 M KCl for 2 min, once with 1 ml 0.1 M Na<sub>2</sub>CO<sub>3</sub> for ~10 s, once with 1 ml 2 M urea in 10 mM Tris-HCl (pH 8.0) for ~10 s, and again twice with 1 ml lysis buffer for 2 min.

#### In-solution tryptic digestion for mass spectrometry

The samples were heated at 95°C in elution buffer [12 mM sodium lauroyl sarcosine, 0.5% sodium deoxycholate, 50 mM triethylammonium bicarbonate (TEAB) containing tris(2-carboxyethyl)phosphine (10 mM) and chloroacetamide (40 mM)] for 20 min. The samples were then diluted 5-fold with 50 mM TEAB and digested with trypsin (1 µg) for 16 hours at 37°C. A 1:1 (volume/volume) ratio of ethyl acetate plus 1% trifluoroacetic acid (TFA) was added to the samples and samples were vortexed for 5 min. Samples were centrifuged at 16000g for 5 min at room temperature and the supernatant was discarded. The samples were desalted using a modified version of Rappsilber's protocol (91) in which the dried samples were reconstituted in acetonitrile/ water/TFA (solvent A, 100 μl, 2/98/0.1, v/v/v) and then loaded onto a small portion of a C18-silica disk (3M, Maplewood, MN) placed in a 200 µl pipette tip. Prior to sample loading the C18 disk was prepared by sequential treatment with methanol (20 µl), acetonitrile/water/TFA (solvent B, 20  $\mu$ l, 80/20/0.1, v/v/v) and finally with solvent A (20  $\mu$ l). After loading the sample, the disc was washed with solvent A (20  $\mu$ l, eluent discarded) and eluted with solvent B (40 µl). The collected eluent was dried in a centrifugal vacuum concentrator and reconstituted in 0.1% Formic Acid (10 µl) for LC-MS/MS analysis.

#### LC-MS/MS analysis

Aliquots of each sample (5  $\mu$ l) were injected onto a reverse phase nanobore HPLC column (AcuTech Scientific, C18, 1.8 $\mu$ m particle size, 360  $\mu$ m  $\times$  20 cm, 150  $\mu$ m ID), equilibrated in solvent A (water/acetonitrile/ FA, 98/2/0.1, v/v/v) and eluted (300 nl/minute) with an increasing

Science 9 OCTOBER 2025 17 of 21

concentration of solvent B (acetonitrile/water/FA, 98/2/0.1, v/v/v: min/% F; 0/0, 5/3, 18/7, 74/12, 144/24, 153/27, 162/40, 164/80, 174/80, 176/0, 180/0) using an EASY-nLC II (Thermo Fisher Scientific). The effluent from the column was directed to a nanospray ionization source connected to a hybrid quadrupole-Orbitrap mass spectrometer (Q Exactive Plus, Thermo Fisher Scientific) acquiring mass spectra in a data-dependent mode alternating between a full scan (m/z 350-1700, automated gain control (AGC) target  $3\times10^6$ , 50 ms maximum injection time, FWHM resolution 70,000 at m/z 200) and up to 15 MS/MS scans (quadrupole isolation of charge states 2-7, isolation window 0.7 m/z) with previously optimized fragmentation conditions (normalized collision energy of 32, dynamic exclusion of 30 s, AGC target  $1\times10^5$ , 100 ms maximum injection time, FWHM resolution 35,000 at m/z 200).

#### **Protein identification**

For experimental mass spectrometry data acquisition and analysis workflow, the raw proteomic data were searched against a Uniprot database containing the complete mouse proteome using SEQUEST-HT (Version 2.4, Thermo Scientific), which provided measurements of relative abundance of the identified peptides. Decoy database searching was used to generate high confidence tryptic peptides (FDR <1%). Tryptic peptides containing amino acid sequences unique to individual proteins were used to identify and provide relative quantification between different proteins in each sample. We performed protein identification of all treatment conditions in both empty vector (TurboID only) and TurboID-Aster-A expressing cells. This approach enhanced confidence in identifying proximity associations. Potential non-specific associations were defined as proteins identified in substantial abundance in both control TurboID only and in experimental groups and were excluded from further analysis. The remaining protein abundance was compared between experimental conditions and ranked as shown in Fig. 5B and in data S3.

# TurbolD biotinylated protein IP and protein coimmunoprecipitation (co-IP)

Confirmation of MS results in cholesterol depletion/repletion conditions were performed as described above using 300-500  $\mu g$  total protein. In TurboID labeling involving TCR activation, EL-4 cells are either cultured in 10% FCS complete media or pre-treated with DMSO or 50  $\mu M$  BAPTA for 20 min at 37°C. Then cells were added to prewarmed culture plate precoated with 5  $\mu g/ml$  anti-CD3/CD28 with or without 10 mM EGTA. The plate was centrifuged at 1,200 rpm for 1 min to facilitate cell attachment and TCR activation for 1 hour. For ionomycin treatment, 1  $\mu M$  ionomycin was added to cells plated on non-coated culture plates for 1 hour. For all experiments, 50  $\mu M$  biotin was added to the culture media for the last 30 min to facilitate labeling. Proteins were eluted by boiling beads in 30  $\mu l$  3X LDS loading buffer containing 2 mM free biotin and 20 mM DTT on a shaking thermo block (1,000 rpm) at 95°C for 10 min. For input control, 30  $\mu g$  cleared lysate prior to beads incubation was diluted in 1X LDS loading buffer with 20 mM DTT.

Stable polyclonal EL-4 lines expressing HA empty vector, HA-mAster-A (WT), HA-mAster-A (R186W) or co-expression with Myc-mSTIM1 were constructed as above and treated in cholesterol replete or deplete conditions as described in the TurboID biotinylated protein IP section. After 1 hour treatment, cells were collected by centrifugation at 1,200 rpm, 5 min at 4°C and washed extensively with cold PBS. Cell pellets were then incubated with IP lysis buffer [20 mM Tris-HCl, 2 mM EDTA, 135 mM NaCl, 10% (vol/vol) glycerol, 0.5% Igepal CA-630, 2X Halt protease inhibitor cocktail, 2 mM PMSF, pH 7.5] for 30 min at 4°C with gentle rotation. Lysates are further sonicated with 20% amplitude, 3 cycles of 5 s on, 10 s off and insoluble fraction was removed by centrifugation at 12,000 xg for 15 min. Protein concentration was determined by BCA assay and 1 mg total protein was precleared with protein A/G PLUS beads (Santa Cruz Biotechnology) for 1 hour at 4°C. Cleared lysates were incubated with 10 µg mouse Anti-HA (16B2) overnight

at  $4^{\circ}\text{C}$  with gentle rotation. Antibody bound proteins were precipitated with protein A/G PLUS beads (Santa Cruz Biotechnology) for 3-4 hours at  $4^{\circ}\text{C}$  while rotating. A/G beads were washed five times, 10 min each with 1x co-IP lysis buffer and proteins were eluted by incubating A/G beads in 20-40  $\mu$ l 3X SDS sample buffer at 95°C for 10 min with 1,000 rpm shaking. Antibodies against HA Tag, STIM1, mouse Aster-A, or Myc Tag were used for immunoblotting.

# Sample preparation and library construction for bulk mRNA sequencing

Small intestine lamina propria mononuclear cells were isolated using the method described above. One micromolar flavopiridol (RNA polymerase inhibitor) was included in all digestion steps to halt de novo transcription of stress-related genes as a result of tissue dissociation. Single cell suspension was FACS-gated on Single/Live cell/CD45 $^+$ /CD90 $^+$ /CD3 $^+$  and sorted into CD4 $^+$  and CD8 $^+$  populations directly into 700  $\mu$ l Trizol LS reagent. Sorting strategy is shown in fig. S21A. Total RNA was extracted using TRIzol and the miRNeasy Mini Kit with oncolumn DNase I digestion (Qiagen).

RNA library preparations and sequencing reactions were conducted at GENEWIZ, LLC. RNA samples were quantified using Qubit 2.0 Fluorometer (Life Technologies) and RNA integrity was checked using Agilent TapeStation 4200 (Agilent Technologies). RNA sequencing libraries were prepared using the NEBNext Ultra II RNA Library Prep Kit for Illumina using manufacturer's instructions. Briefly, poly-A mRNAs were initially enriched with Oligo dT beads. Enriched mRNAs were fragmented for 15 min at 94°C. First strand and second strand cDNA were subsequently synthesized. cDNA fragments were end repaired and adenylated at 3′ends, and universal adapters were ligated to cDNA fragments, followed by index addition and library enrichment by PCR with limited cycles. The sequencing library was validated on the Agilent TapeStation (Agilent Technologies) and quantified by using Qubit 4.0 Fluorometer (Invitrogen) as well as by quantitative PCR (KAPA Biosystems).

#### **Bulk mRNA sequencing and analysis**

The sequencing libraries were clustered on flowcells. After clustering, the flowcells were loaded on the Illumina HiSeq instrument (4000 or equivalent) according to manufacturer's instructions. The samples were sequenced using a 2x150bp Paired End configuration. Image analysis and base calling were conducted by the HiSeq Control Software (HCS). Raw sequence data (.bcl files) generated from Illumina HiSeq was converted into fastq files and de-multiplexed using Illumina's bcl2fastq 2.17 software. One mismatch was allowed for index sequence identification. Adapter and quality trimming of raw FASTQ files was performed using Trimmomatic. FastQC was used to perform quality control of the FASTQ files before and after trimming. Trimmed FASTQ files were aligned to GRCm38/mm10 using STAR package. HTSeq-count was used to extract gene counts and differential gene expression analysis was performed using DESeq2 package (doi:10.1186/s13059-014-0550-8) in R 4.1.1. Normalized gene expression of the individual samples is shown in data S1 and differentially expressed gene list is shown in data S2.

#### Single-cell RNA sequencing

Small intestine lamina propria mononuclear cells were isolated using the method described in the bulk mRNA sequencing section. Single Live EPCAM Ter119 CD31 CD45 cells were sorted from 10- to 12-week-old female littermates on a BD Aria FACS sorter. Sorting strategy is shown in fig. S23. Then, 100,000 cells were sorted from each mouse (n=3/genotype) and pooled together before loading to a Chromium Single Cell Controller (10X Genomics). Libraries were prepared using a 10X Genomics 3′GEX Kits following the manufacturer's protocols. Libraries were then sequenced on an Illumina NovaSeq S2 using  $2 \times 50$  bp paired end sequencing with a targeted depth of 50,000 read pairs per cell.

Science 9 OCTOBER 2025 18 of 21

Raw reads were aligned to mouse mm10 genome using CellRanger (v7.2.0). Counts from ambient RNA was removed using CellBender [(v0.3.0); Github: broadinstitute/CellBender] and doublets were removed using scDblFinder [(v1.18.0); DOI: 10.18129/B9.bioc.scDblFinder]. Preprocessing was performed using Seurat [(v5.0.1); Github: satijalab/ seurat] in R 4.3.1. Specifically, we filtered for cells with 500<nUMI <30000, 200<nGenes <10000 and percent.MT < 5%. Normalization was done using SCTransform with percent.MT regressed out. Initial data integration was done using the SelectIntegrationFeatures(), PrepSCTIntegration(), FindIntegrationAnchors () and IntegrateData() functions with RPCA method and 3000 variable features. Dimensional reduction was done using top 50 principal components (PCs) and subsequent Harmony integration. Visualization was performed using RunUMAP() function. Cell clustering was performed using the FindNeighbors() function (50 harmony embeddings, k = 35) and FindClusters() function with igraph and Leiden method (resolution = 0.6). To isolate lymphoid lineage for further analysis, we subset clusters expressing Thy1 (CD90) from the original Seurat object. The same normalization and integration procedure was applied to lymphoid lineage clusters. To identify stable clusters, we performed bootstrapping of 80% of the cells 20 times, and tested stability of clusters from a wide range of parameters, including number of PCs used, k parameters in FindNeighbors() and resolution in FindClusters(). We decided to use 20 top PCs, k = 30 and resolution = 0.8 to maximizing cluster diversity while maintaining cluster stability. Cluster markers were identified using FindMarkers() function and manual annotation was performed using established cell markers. Cluster were manually annotated based on matching cluster markers (fig. S17A, list of markers is shown in data S4) with cell type ULI RNA-seq data in the Immgen database and previously published small intestine mononuclear cell single-cell RNA sequencing results (GSE124880).

# Access and analysis of previously published gene expression and sequencing datasets

Tissue panel gene expression (fig. S1E) was analyzed in BioGPS repository from aggregated datasets GSE1133, GSE10246, GSE15998. Immune cell expression panel (fig. S1G) was obtained from ImmGen ULI RNA-seq data (GSE109125 and GSE127267). Human single cell meta-analysis (fig. S9, A and B) was performed using Swiss Portal for Immune Cell Analysis and scIBD database (92, 93). ChIP-seq data (fig. S9F) was analyzed in Cistrome database using datasets GSM978770, GSM978769, GSM978772, GSM1126691, GSM2706520, GSM2387500. Sequencing tracks were visualized with Integrated Genome Viewer (2.16.2).

#### Statistical analysis

Data in all figures are representative of or pooled from at least two independent experiments or as indicated in the figure legends. Data are shown as Mean  $\pm$  SEM. For experiments involving wildtype mice or mice of the same genotype, groups were assigned so that control and treatment groups have similar average body weight. In Cre-flox system or WT-KO genotypes, balanced numbers of littermate mice were used where possible and randomly assigned to experimental groups. Samples were processed in an order that alternated between WT/KO or control/treatment subjects. Formal blinding was not applied when performing the experiments or analyzing the data. Power calculations were not applied to predetermine sample size. Sample size was based on prior laboratory practice and literature reports on similar assays. Groups were compared using Prism software (v10.3.0). For statistics tests requiring normal distribution, datasets were first tested for normality and log normality using Kolmogorov-Smirnov test. If data distribution was not normal, it was first log-transformed, tested again using Kolmogorov-Smirnov for normality, before proceeding with the corresponding statistical tests. The statistical methods and correction used for each experiment are reported in the corresponding figure captions.

#### **REFERENCES AND NOTES**

- A. Das, M. S. Brown, D. D. Anderson, J. L. Goldstein, A. Radhakrishnan, Three pools of plasma membrane cholesterol and their relation to cholesterol homeostasis. *eLife* 3, e02882 (2014). doi: 10.7554/eLife.02882; pmid: 24920391
- S. Endapally et al., Molecular discrimination between two conformations of sphingomyelin in plasma membranes. Cell 176, 1040–1053.e17 (2019). doi: 10.1016/j.cell.2018.12.042; pmid: 30712872
- S. Endapally, R. E. Infante, A. Radhakrishnan, Monitoring and modulating intracellular cholesterol trafficking using ALOD4, a cholesterol-binding protein. *Methods Mol. Biol.* 1949, 153–163 (2019). doi: 10.1007/978-1-4939-9136-5\_12; pmid: 30790255
- K. A. Johnson, A. Radhakrishnan, The use of anthrolysin O and ostreolysin A to study cholesterol in cell membranes. *Methods Enzymol.* 649, 543–566 (2021). doi: 10.1016/bs. mie.2021.01.011; pmid: 33712199
- A. Ferrari et al., Aster proteins regulate the accessible cholesterol pool in the plasma membrane. Mol. Cell. Biol. 40, e00255-e20 (2020). doi: 10.1128/MCB.00255-20; pmid: 32719109
- X. Xiao et al., Hepatic nonvesicular cholesterol transport is critical for systemic lipid homeostasis. Nat. Metab. 5, 165–181 (2023). doi: 10.1038/s42255-022-00722-6; pmid: 36646756
- Q. D. Zhou et al., Interferon-mediated reprogramming of membrane cholesterol to evade bacterial toxins. Nat. Immunol. 21, 746–755 (2020). doi: 10.1038/s41590-020-0695-4; pmid: 32514064
- M. Kinnebrew et al., Patched 1 reduces the accessibility of cholesterol in the outer leaflet of membranes. eLife 10, e70504 (2021). doi: 10.7554/eLife.70504; pmid: 34698632
- M. E. Abrams et al., Oxysterols provide innate immunity to bacterial infection by mobilizing cell surface accessible cholesterol. Nat. Microbiol. 5, 929–942 (2020). doi: 10.1038/ s41564-020-0701-5; pmid: 32284563
- M. N. Trinh et al., Interplay between Asters/GRAMD1s and phosphatidylserine in intermembrane transport of LDL cholesterol. Proc. Natl. Acad. Sci. U.S.A. 119, e2120411119 (2022). doi: 10.1073/pnas.2120411119; pmid: 34992143
- M.-S. Lee, S. J. Bensinger, Reprogramming cholesterol metabolism in macrophages and its role in host defense against cholesterol-dependent cytolysins. *Cell. Mol. Immunol.* 19, 327–336 (2022). doi: 10.1038/s41423-021-00827-0; pmid: 35017717
- J. Sandhu et al., Aster proteins facilitate nonvesicular plasma membrane to ER cholesterol transport in mammalian cells. Cell 175, 514–529.e20 (2018). doi: 10.1016/j. cell.2018.08.033; pmid: 30220461
- C. He et al., Macrophages release plasma membrane-derived particles rich in accessible cholesterol. Proc. Natl. Acad. Sci. U.S.A. 115, E8499–E8508 (2018). doi: 10.1073/ pnas.1810724115; pmid: 30127022
- X. Hu et al., Release of cholesterol-rich particles from the macrophage plasma membrane during movement of filopodia and lamellipodia. eLife 8, e50231 (2019). doi: 10.7554/ el.ife.50231: pmid: 31486771
- A. Ferrari et al., Aster-dependent nonvesicular transport facilitates dietary cholesterol uptake. Science 382, eadf0966 (2023). doi: 10.1126/science.adf0966; pmid: 37943936
- M. Kinnebrew et al., Cholesterol accessibility at the ciliary membrane controls hedgehog signaling. eLife 8, e50051 (2019). doi: 10.7554/eLife.50051; pmid: 31657721
- E. Ikonen, V. M. Olkkonen, Intracellular cholesterol trafficking. Cold Spring Harb. Perspect. Biol. 15, 041404 (2023). pmid: 37277190
- J. P. Kennelly, P. Tontonoz, Cholesterol transport to the endoplasmic reticulum. Cold Spring Harb. Perspect. Biol. 15, 041263 (2023). pmid: 35940908
- T. Naito et al., Movement of accessible plasma membrane cholesterol by the GRAMD1 lipid transfer protein complex. eLife 8, e51401 (2019). doi: 10.7554/eLife.51401; pmid: 31724953
- X. Xiao et al., Aster-B-dependent estradiol synthesis protects female mice from diet-induced obesity. J. Clin. Invest. 134, e173002 (2024). doi: 10.1172/JCI173002; pmid: 38175723
- F. Wang, K. Beck-García, C. Zorzin, W. W. A. Schamel, M. M. Davis, Inhibition of T cell receptor signaling by cholesterol sulfate, a naturally occurring derivative of membrane cholesterol. *Nat. Immunol.* 17, 844–850 (2016). doi: 10.1038/ni.3462; pmid: 27213689
- E. Molnár et al., Cholesterol and sphingomyelin drive ligand-independent T-cell antigen receptor nanoclustering. J. Biol. Chem. 287, 42664–42674 (2012). doi: 10.1074/jbc. M112.386045; pmid: 23091059
- 23. M. Hose et al., Cell-intrinsic ceramides determine T cell function during melanoma progression. eLife 11, e83073 (2022). doi: 10.7554/eLife.83073; pmid: 36426850
- 24. J. Yuan et al., Potentiating CD8<sup>+</sup>T cell antitumor activity by inhibiting PCSK9 to promote LDLR-mediated TCR recycling and signaling. Protein Cell 12, 240–260 (2021). doi: 10.1007/s13238-021-00821-2; pmid: 33606190
- W. Yang et al., Potentiating the antitumour response of CD8<sup>+</sup>T cells by modulating cholesterol metabolism. Nature 531, 651–655 (2016). doi: 10.1038/nature17412; pmid: 26982734
- W. W. A. Schamel, B. Alarcon, T. Höfer, S. Minguet, The allostery model of TCR regulation.
   J. Immunol. 198, 47–52 (2017). doi: 10.4049/jimmunol.1601661; pmid: 27994168
- Y. Chen et al., Cholesterol inhibits TCR signaling by directly restricting TCR-CD3 core tunnel motility. Mol. Cell 82, 1278–1287.e5 (2022). doi: 10.1016/j.molcel.2022.02.017; pmid: 35271814

Science 9 OCTOBER 2025 19 of 21

#### **RESEARCH ARTICLE**

- B. Wang et al., Intestinal phospholipid remodeling is required for dietary-lipid uptake and survival on a high-fat diet. Cell Metab. 23, 492–504 (2016). doi: 10.1016/ j.cmet.2016.01.001; pmid: 26833026
- J. P. Kennelly et al., Intestinal de novo phosphatidylcholine synthesis is required for dietary lipid absorption and metabolic homeostasis. J. Lipid Res. 59, 1695–1708 (2018). doi: 10.1194/jlr.M087056; pmid: 30007917
- D. H. Z. Koh *et al.*, Visualization of accessible cholesterol using a GRAM domain-based biosensor. *Nat. Commun.* 14, 6773 (2023). doi: 10.1038/s41467-023-42498-7; pmid: 37880244
- T. Naito, M. Na, D. H. Z. Koh, Y. Saheki, "Using GRAM domain-based biosensors to monitor accessible cholesterol distribution in live cells" in *Intracellular Lipid Transport: Methods* and *Protocols*, *Methods in Molecular Biology*, vol. 2888, G. Drin, Ed. (Springer, 2025), pp. 67–82.doi: 10.1007/978-1-0716-4318-1\_6
- M. Doktorova et al., Cell membranes sustain phospholipid imbalance via cholesterol asymmetry. Cell 188, 2586–2602.e24 (2025). doi: 10.1016/j.cell.2025.02.034; pmid: 40179882
- D. Sputay et al., Immune cell activation produces locally scrambled foci of plasma membrane lipids. Faraday Discuss. 259, 45–59 (2025). doi: 10.1039/D4FD00205A; pmid: 40351229
- 34. K. Fischer et al., Antigen recognition induces phosphatidylserine exposure on the cell surface of human CD8<sup>+</sup> T cells. Blood 108, 4094–4101 (2006). doi: 10.1182/blood-2006-03-011742; pmid: 16912227
- Y. Hu et al., Scramblase TMEM16F terminates T cell receptor signaling to restrict T cell exhaustion. J. Exp. Med. 213, 2759–2772 (2016). doi: 10.1084/jem.20160612; pmid: 27810927
- J. Suzuki, M. Umeda, P. J. Sims, S. Nagata, Calcium-dependent phospholipid scrambling by TMEM16F. Nature 468, 834–838 (2010). doi: 10.1038/nature09583; pmid: 21107324
- S. Feng et al., Identification of a drug binding pocket in TMEM16F calcium-activated ion channel and lipid scramblase. Nat. Commun. 14, 4874 (2023). doi: 10.1038/s41467-023-40410-x; pmid: 37573365
- S. Pathan-Chhatbar et al., Direct regulation of the T cell antigen receptor's activity by cholesterol. Front. Cell Dev. Biol. 8, 615996 (2021). doi: 10.3389/fcell.2020.615996; pmid: 33490080
- M. Swamy, W. W. A. Schamel, Purification of the T cell antigen receptor and analysis by blue-native PAGE. Methods Mol. Biol. 514, 135–150 (2009). doi: 10.1007/978-1-60327-527-9\_10; pmid: 19048218
- E. Esplugues et al., Control of T<sub>H</sub>17 cells occurs in the small intestine. Nature 475, 514–518 (2011). doi: 10.1038/nature10228; pmid: 21765430
- K. F. Cho et al., Proximity labeling in mammalian cells with TurbolD and split-TurbolD. Nat. Protoc. 15, 3971–3999 (2020). doi: 10.1038/s41596-020-0399-0; pmid: 33139955
- T. Balla, G. Gulyas, Y. J. Kim, J. Pemberton, Phosphoinositides and calcium signaling. A marriage arranged in ER-PM contact sites. *Curr. Opin. Physiol.* 17, 149–157 (2020). doi: 10.1016/j.cophys.2020.08.007; pmid: 32944676
- Y.-J. Chen, C. G. Quintanilla, J. Liou, Recent insights into mammalian ER-PM junctions. Curr. Opin. Cell Biol. 57, 99–105 (2019). doi: 10.1016/j.ceb.2018.12.011; pmid: 30739879
- 44. W. Y. Chung, A. Jha, M. Ahuja, S. Muallem, Ca<sup>2+</sup> influx at the ER/PM junctions. *Cell Calcium* **63**, 29–32 (2017). doi: 10.1016/j.ceca.2017.02.009; pmid: 28262262
- P. G. Hogan, R. S. Lewis, A. Rao, Molecular basis of calcium signaling in lymphocytes: STIM and ORAI. Annu. Rev. Immunol. 28, 491–533 (2010). doi: 10.1146/annurev. immunol.021908.132550; pmid: 20307213
- Y. Saheki, P. De Camilli, Endoplasmic reticulum-plasma membrane contact sites. *Annu. Rev. Biochem.* 86, 659–684 (2017). doi: 10.1146/annurev-biochem-061516-044932; pmid: 28301744
- 47. V. A. Barr et al., Dynamic movement of the calcium sensor STIM1 and the calcium channel Orai1 in activated T-cells: Puncta and distal caps. Mol. Biol. Cell 19, 2802–2817 (2008). doi: 10.1091/mbc.e08-02-0146; pmid: 18448669
- 48. W.-W. Shen, M. Frieden, N. Demaurex, Local cytosolic Ca<sup>2+</sup> elevations are required for stromal interaction molecule 1 (STIM1) de-oligomerization and termination of store-operated Ca<sup>2+</sup> entry. J. Biol. Chem. 286, 36448–36459 (2011). doi: 10.1074/jbc. M111.269415; pmid: 21880734
- B. Ercan, T. Naito, D. H. Z. Koh, D. Dharmawan, Y. Saheki, Molecular basis of accessible plasma membrane cholesterol recognition by the GRAM domain of GRAMD1b. *EMBO J.* 40, e106524 (2021). doi: 10.15252/embj.2020106524; pmid: 33604931
- U. Kaufmann et al., Calcium signaling controls pathogenic Th17 cell-mediated inflammation by regulating mitochondrial function. Cell Metab. 29, 1104–1118.e6 (2019). doi: 10.1016/j.cmet.2019.01.019; pmid: 30773462
- S. Kahlfuss et al., STIM1-mediated calcium influx controls antifungal immunity and the metabolic function of non-pathogenic Th17 cells. EMBO Mol. Med. 12, e11592 (2020). doi: 10.15252/emmm.201911592; pmid: 32609955
- 52. B. Wu, J. S. Woo, Z. Sun, S. Srikanth, Y. Gwack, Ca<sup>2+</sup> signaling augmented by ORAl1 trafficking regulates the pathogenic state of effector T cells. *J. Immunol.* **208**, 1329–1340 (2022). doi: 10.4049/jimmunol.2100871; pmid: 35217583
- A. Gay, D. Rye, A. Radhakrishnan, Switch-like responses of two cholesterol sensors do not require protein oligomerization in membranes. *Biophys. J.* 108, 1459–1469 (2015). doi: 10.1016/j.bpj.2015.02.008; pmid: 25809258

- M. Keir, Y. Yi, T. Lu, N. Ghilardi, The role of IL-22 in intestinal health and disease. *J. Exp. Med.* 217, e20192195 (2020). doi: 10.1084/jem.20192195; pmid: 32997932
- 55. R. Basu et al., Th22 cells are an important source of IL-22 for host protection against enteropathogenic bacteria. *Immunity* 37, 1061–1075 (2012). doi: 10.1016/ j.immuni.2012.08.024; pmid: 23200827
- I. I. Ivanov et al., Induction of intestinal Th17 cells by segmented filamentous bacteria. Cell 139, 485–498 (2009). doi: 10.1016/j.cell.2009.09.033; pmid: 19836068
- Y. Yang et al., Focused specificity of intestinal TH17 cells towards commensal bacterial antigens. Nature 510, 152–156 (2014). doi: 10.1038/nature13279; pmid: 24739972
- Y. Goto et al., Segmented filamentous bacteria antigens presented by intestinal dendritic cells drive mucosal Th17 cell differentiation. *Immunity* 40, 594–607 (2014). doi: 10.1016/j.immuni.2014.03.005; pmid: 24684957
- J. Talbot et al., Feeding-dependent VIP neuron-ILC3 circuit regulates the intestinal barrier.
   Nature 579, 575–580 (2020). doi: 10.1038/s41586-020-2039-9; pmid: 32050257
- K. Mao et al., Innate and adaptive lymphocytes sequentially shape the gut microbiota and lipid metabolism. Nature 554, 255–259 (2018). doi: 10.1038/nature25437; pmid: 29364878
- Z. A. Sullivan et al., γ8 T cells regulate the intestinal response to nutrient sensing. Science 371, eaba8310 (2021). doi: 10.1126/science.aba8310; pmid: 33737460
- 62. Y. Kawano et al., Microbiota imbalance induced by dietary sugar disrupts immunemediated protection from metabolic syndrome. Cell 185, 3501–3519.e20 (2022). doi: 10.1016/j.cell.2022.08.005; pmid: 36041436
- X. Wang et al., Interleukin-22 alleviates metabolic disorders and restores mucosal immunity in diabetes. Nature 514, 237–241 (2014). doi: 10.1038/nature13564; pmid: 25119041
- L. A. Zenewicz et al., IL-22 deficiency alters colonic microbiota to be transmissible and colitogenic. J. Immunol. 190, 5306–5312 (2013). doi: 10.4049/jimmunol.1300016; pmid: 23585682
- Y. Wang et al., The intestinal microbiota regulates body composition through NFIL3 and the circadian clock. Science 357, 912–916 (2017). doi: 10.1126/science.aan0677; pmid: 28860383
- 66. F. Bäckhed, J. K. Manchester, C. F. Semenkovich, J. I. Gordon, Mechanisms underlying the resistance to diet-induced obesity in germ-free mice. *Proc. Natl. Acad. Sci. U.S.A.* 104, 979–984 (2007). doi: 10.1073/pnas.0605374104; pmid: 17210919
- 67. T.Y. Chang, C. C.Y. Chang, D. Cheng, Acyl-coenzyme A:cholesterol acyltransferase. *Annu. Rev. Biochem.* 66, 613–638 (1997). doi: 10.1146/annurev.biochem.66.1.613; pmid: 9242919
- 68. N. M. Schmidt et al., Targeting human Acyl-CoA:cholesterol acyltransferase as a dual viral and T cell metabolic checkpoint. Nat. Commun. 12, 2814 (2021). doi: 10.1038/ s41467-021-22967-7; pmid: 33990561
- K. T. Kennewick, S. J. Bensinger, Decoding the crosstalk between mevalonate metabolism and T cell function. *Immunol. Rev.* 317, 71–94 (2023). doi: 10.1111/imr.13200; pmid: 36999733
- Y. Kidani et al., Sterol regulatory element-binding proteins are essential for the metabolic programming of effector T cells and adaptive immunity. Nat. Immunol. 14, 489–499 (2013). doi: 10.1038/ni.2570; pmid: 23563690
- E. L. Huttlin et al., Dual proteome-scale networks reveal cell-specific remodeling of the human interactome. Cell 184, 3022–3040.e28 (2021). doi: 10.1016/j.cell.2021.04.011; pmid: 33961781
- 72. C. D. Go et al., A proximity-dependent biotinylation map of a human cell. Nature 595, 120–124 (2021). doi: 10.1038/s41586-021-03592-2; pmid: 34079125
- M. Besprozvannaya et al., GRAM domain proteins specialize functionally distinct ER-PM contact sites in human cells. eLife 7, e31019 (2018). doi: 10.7554/eLife.31019; pmid: 29469807
- M. N. Trinh et al., Last step in the path of LDL cholesterol from lysosome to plasma membrane to ER is governed by phosphatidylserine. Proc. Natl. Acad. Sci. U.S.A. 117, 18521–18529 (2020). doi: 10.1073/pnas.2010682117; pmid: 32690708
- W. M. Henne, J. Liou, S. D. Emr, Molecular mechanisms of inter-organelle ER-PM contact sites. *Curr. Opin. Cell Biol.* 35, 123–130 (2015). doi: 10.1016/j.ceb.2015.05.001; pmid: 26025028
- X. Cao et al., The ER/PM microdomain, PI(4,5)P<sub>2</sub> and the regulation of STIM1-Orai1 channel function. Cell Calcium 58, 342–348 (2015). doi: 10.1016/j.ceca.2015.03.003; pmid: 25843208
- W.Y. Chung et al., PtdSer as a signaling lipid determined by privileged localization of ORP5 and ORP8 at ER/PM junctional foci to determine PM and ER PtdSer/PI(4)P ratio and cell function. Proc. Natl. Acad. Sci. U.S.A. 120, e2301410120 (2023). doi: 10.1073/ pnas.2301410120; pmid: 37607230
- G. Gulyas et al., LIPID transfer proteins regulate store-operated calcium entry via control
  of plasma membrane phosphoinositides. Cell Calcium 106, 102631 (2022). doi: 10.1016/
  j.ceca.2022.102631; pmid: 35853265
- M. Reina-Campos et al., Metabolic programs of T cell tissue residency empower tumour immunity. Nature 621, 179–187 (2023). doi: 10.1038/s41586-023-06483-w; pmid: 37648857
- A. H. Pollock et al., Prolonged intake of dietary lipids alters membrane structure and T cell responses in LDLr<sup>-/-</sup> mice. J. Immunol. 196, 3993–4002 (2016). doi: 10.4049/ jimmunol.1501261; pmid: 27183636

Science 9 OCTOBER 2025 20 of 21

- R. K. W. Mailer, A. Gisterå, K. A. Polyzos, D. F. J. Ketelhuth, G. K. Hansson, Hypercholesterolemia enhances T cell receptor signaling and increases the regulatory T cell population. Sci. Rep. 7, 15655 (2017). doi: 10.1038/s41598-017-15546-8; pmid: 29142309
- Q. Gao et al., A critical function of Th17 proinflammatory cells in the development of atherosclerotic plaque in mice. J. Immunol. 185, 5820–5827 (2010). doi: 10.4049/ immunol.1000116; pmid: 20952673
- 83. Y. U. Kim, P. Kee, D. Danila, B.-B. Teng, A critical role of PCSK9 in mediating IL-17-producing T cell responses in hyperlipidemia. *Immune Netw.* **19**, e41 (2019). doi: 10.4110/in.2019.19. e41; pmid: 31921471
- 84. Y. Wang et al., Interleukin-17-producing CD4<sup>+</sup> T cells promote inflammatory response and foster disease progression in hyperlipidemic patients and atherosclerotic mice. Front. Cardiovasc. Med. 8, 667768 (2021). doi: 10.3389/fcvm.2021.667768; pmid: 33981738
- R. Saigusa, H. Winkels, K. Ley, T cell subsets and functions in atherosclerosis. Nat. Rev. Cardiol. 17, 387–401 (2020). doi: 10.1038/s41569-020-0352-5; pmid: 32203286
- 86. S. Omenetti et al., The intestine harbors functionally distinct homeostatic tissue-resident and inflammatory Th17 cells. *Immunity* 51, 77–89.e6 (2019). doi: 10.1016/ j.immuni.2019.05.004; pmid: 31229354
- 87. C. L. Zindl *et al.*, A nonredundant role for T cell-derived interleukin 22 in antibacterial defense of colonic crypts. *Immunity* **55**, 494–511.e11 (2022). doi: 10.1016/j.immuni.2022.02.003; pmid: 35263568
- A. I. Mina et al., CalR: A web-based analysis tool for indirect calorimetry experiments. Cell Metab. 28, 656–666.e1 (2018). doi: 10.1016/j.cmet.2018.06.019; pmid: 30017358
- J. Folch, M. Lees, G. H. Sloane Stanley, A simple method for the isolation and purification of total lipides from animal tissues. *J. Biol. Chem.* 226, 497–509 (1957). doi: 10.1016/ S0021-9258(18)64849-5; pmid: 13428781
- D. R. Stirling et al., CellProfiler 4: Improvements in speed, utility and usability. BMC Bioinformatics 22, 433 (2021). doi: 10.1186/s12859-021-04344-9; pmid: 34507520
- J. Rappsilber, M. Mann, Y. Ishihama, Protocol for micro-purification, enrichment, pre-fractionation and storage of peptides for proteomics using StageTips. *Nat. Protoc.* 2, 1896–1906 (2007). doi: 10.1038/nprot.2007.261; pmid: 17703201
- 92. H. Nie et al., Single-cell meta-analysis of inflammatory bowel disease with scIBD. Nat. Comput. Sci. 3, 522–531 (2023). doi: 10.1038/s43588-023-00464-9; pmid: 38177426
- M. Andreatta, F. P. A. David, C. Iseli, N. Guex, S. J. Carmona, SPICA: Swiss portal for immune cell analysis. *Nucleic Acids Res.* 50, D1109–D1114 (2022). doi: 10.1093/nar/gkab1055; pmid: 34747477
- Y. Gao, P. Tontonoz, W. Cohn, J. Whitelegge, T cell cholesterol transport links intestinal immune responses to dietary lipid absorption. Dryad (2025); https://doi.org/10.5061/ dryad.w9ghx3g31.

#### **ACKNOWLEDGMENTS**

We thank all members of the Tontonoz, Tarling-Vallim, Mack, Young, and Bensinger labs at University of California, Los Angeles (UCLA) for advice and discussions and for sharing

reagents and resources. pALOD4 and pOlyA were a gift from A. Radhakrishnan (UT Southwestern Medical Center), and the  $\it Il22^{hCD4.fl}$  strain was a kind gift from C. L. Zindl, S. N. Harbour, and C. T. Weaver (University of Alabama at Birmingham). We thank the CNSI Microscopy Core, Broad Stem Cell Core Facilities, Flow Cytometry Core, Translational Pathology Core Laboratory, UCLA Microbiome Core, and Technology Center for Genomics and Bioinformatics at UCLA for their service and experimental suggestions. We also thank L. Qi for assisting with scRNA-seq analysis and C. I. Corrales for supporting the generation of TurboID-expressing cell lines. Funding: This work was supported by National Institutes of Health (NIH) grants R01 DK126779 and R01 HL175773 (P.T.); Transatlantic Network of Excellence, Leducq Foundation, 19CDV04 (P.T., S.G.Y.); NIH grant P01 HL146358 (P.T., S.G.Y., S.J.B.); NIH grant R35 HL139725 (S.G.Y.); Damon Runyon Foundation/The Mark Foundation Postdoctoral Fellowship DRG-2424-21, NIH grant K99 DK138289, and, in part, by the UCLA Jonsson Comprehensive Cancer Center's Office of Cancer Training and Education (Y.Ga.); NIH-National Center for Advancing Translational Sciences grant UL1TR001881 (Y.Ga., P.T.); American Heart Association Postdoctoral Fellowship 903306 (J.P.K.); American Heart Association Postdoctoral Fellowship 18POST34030388 and UCSD-UCLA Diabetes Research Center P30 (DK063491) (X.X.); CDI NIH K12 Junior Faculty Career Development Grant (1K12HD111040), Today's and Tomorrow's Children Fund Bridge Grant, and UCLA David Geffen School of Medicine Office of Physician Scientist Career Development Bridge Grant (E.W.); University of California, San Diego (UCSD)-UCLA Diabetes Research Center P30 (DK063491) (E.W., P.T.): American Diabetes Association Postdoctoral fellowship 1-19-PDF-043-RA and Ermenegildo Zegna Founder's Scholarship 2017 (A.F.); NIH grants T32 DK007180 and K08DK136706 (A.H.N.); NIH grant F30 DK134050 and UCLA-Caltech Medical Scientist Training Program T32 GM008042 (L.F.U.); and NIH grants R01Al146615 (Y.Gw.) and R01Al146352 (S.S.). Author contributions: Conceptualization: Y.Ga., J.P.K., P.T.; Methodology: Y.Ga., J.P.K., X.X., A.H.B., S.S., T.W., A.N., W.C.; Investigation: Y.Ga., J.P.K., X.X., E.W., A.F., J.J.M., S.S., D.H.C., T.W., L.F.U.; Visualization: Y.Ga., J.P.K., X.X., A.H.B., T.W., J.J.M., S.S.; Funding acquisition: Y.Ga., P.T.; Project administration: Y.Ga., P.T.; Supervision: P.T., S.G.Y., J.J.M., S.J.B., S.S., Y.Gw., J.W.; Resources: A.N., M.S.L., S.J.B.; Writing – original draft: Y.Ga., P.T.; Writing – review & editing: Y.Ga., J.P.K., X.X., P.T. Competing interests: All authors declare that they have no competing interests. Data and materials availability: All data needed to evaluate the conclusions in the paper are available in the manuscript or the supplementary materials. Sequencing data generated in this study have been deposited to the Gene Expression Omnibus (GEO) under accession nos. GSE277067 (bulk CD4 RNA-seq) and GSE277138 (scRNA-seq). Proteomics mass spectrometry data generated in this study have been deposited to Dryad (94). The biological materials that were used are readily available from the authors or from standard commercial sources. Aster-A<sup>F/F</sup> mice are available from P.T. under a material agreement with UCLA. License information: Copyright @ 2025 the authors, some rights reserved; exclusive licensee American Association for the Advancement of Science. No claim to original US government works. https://www.science.org/about/ science-licenses-journal-article-reuse

#### SUPPLEMENTARY MATERIALS

science.org/doi/10.1126/science.adt4169
Figs. S1 to S39; Tables S1 to S3; MDAR Reproducibility Checklist; Data S1 to S4; Movie S1
Submitted 26 September 2024; accepted 1 August 2025

10.1126/science.adt4169

Science 9 OCTOBER 2025 21 of 21

#### PHYSIOLOG<sup>3</sup>

# A tripartite alliance for dietary fat absorption

Microbes, immune cells, and enterocytes interact to regulate the intake of lipids in the mouse gut

#### Ralph Burkhardt and Josef Ecker

ietary lipids are a major daily source of calories in adult mammals. The textbook description of lipid absorption is straightforward: Lipids cross the layer of cells lining the gut (the intestinal epithelium) to move from inside the intestinal tract to the blood stream. On page 149 of this issue, Gao *et al.* (*I*) report that lipid absorption in mice also relies on

communication between immune cells and specific intestinal epithelial cells (enterocytes). This relationship is influenced by the gut microbiota, a complex and diverse microbial ecosystem of the intestinal tract (2). Loss of the protein Aster-A in immune cells inhibits lipid absorption and protects mice against diet-induced obesity and its consequences, including adipose tissue inflammation and fatty liver. These findings are likely to be of major interest for research on therapies that target dietary fat absorption.

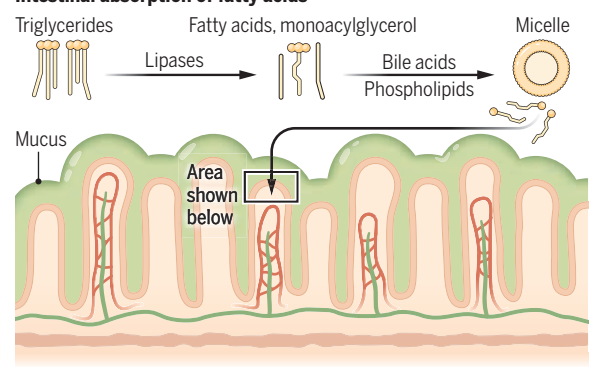
The intestinal epithelium is a physical and biochemical barrier that separates the space inside the gut-the intestinal lumen-from the host tissue (see the figure). Most dietary lipids are triglycerides, which are molecules composed of three fatty acids esterified to a single glycerol backbone. The entry of fatty acids into enterocytes depends on the activity of pancreatic lipase, an enzyme that breaks down triglycerides (3). Monoacylglycerols and free fatty acids are emulsified with bile acids and phospholipids, forming a spherical structure known as a micelle. The biophysical properties of the apical cell membrane of enterocytes, which faces the intestinal lumen, also influence lipid absorption. This membrane is under constant remodeling by enzymes of the lysophosphatidylcholine acyltransferase protein family, which change its phospholipid composition (4). The gut microbiota also plays a role in fatty acid uptake. Mice without gut microbes have higher levels of dietary polyunsaturated fatty acids in the circulation and peripheral tissues compared with mice with a naturally diverse microbiota (5). In humans, the presence of the commensal mucus-degrading bacterium Akkermansia muciniphila has been associated with reduced plasma lipid levels, fat storage, and obesity (6), although the mechanisms underlying these effects are unclear.

The inner layer of the intestinal tract is covered by the mucosa, which contains different regions. Immune cells, which sense microbial stimuli and initiate appropriate responses, can be found within the tissue of the lamina propria and in the Peyer's patches (7). Gao *et al.* observed that T helper 17 (T<sub>H</sub>17) cells, a subset of CD4<sup>+</sup> T cells, express Aster-A, a protein involved in the nonvesicular shuttling of cholesterol

#### Regulation of dietary lipid intake

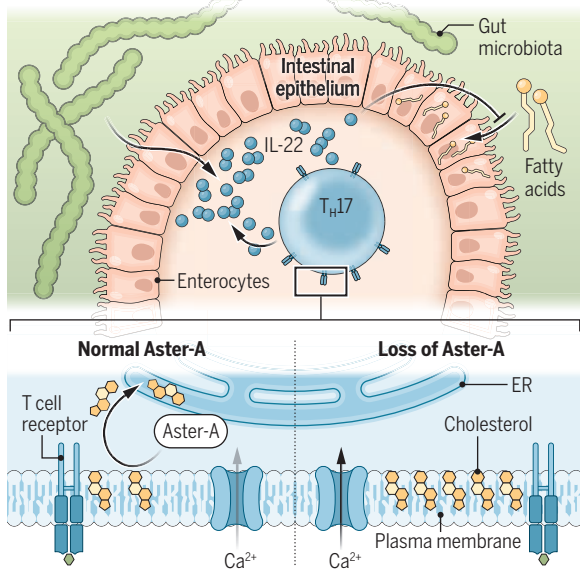
Triglycerides, the main type of dietary lipid, are broken down by lipase enzymes. Fatty acids are emulsified with bile acids and phospholipids, creating spherical structures called micelles. Fatty acids released by micelles are taken in by the enterocytes of the intestinal epithelium.

#### Intestinal absorption of fatty acids



#### Microbes and the immune system control fatty acid intake

Gut microbes stimulate IL-22 production by immune cells. Aster-A shuttles cholesterol between the plasma membrane and the ER in  $T_\mu 17$  cells, which requires  $Ca^{2+}$  influx. Mice without Aster-A in T cells have an increased amount of free cholesterol in the plasma membrane, which stimulates T cell receptor signaling, IL-22 production, and T cell activation and proliferation. An enhanced immune response leads to reduced intestinal absorption of fatty acids by enterocytes and inhibits diet-induced obesity.



ER, endoplasmic reticulum; IL-22, interleukin-22; T<sub>H</sub>17 cells, T helper 17 cells

from the plasma membrane to the endoplasmic reticulum within cells (8). Free cholesterol makes up ~50% of the total lipid content of the plasma membrane of mammalian cells (9). Some of this free-cholesterol pool, referred to as sequestered cholesterol, is required to maintain the membrane's biophysical properties, but another portion, referred to as accessible cholesterol, can be mobilized to other organelles (10). Gao et al. observed that T cell-specific deletion of Aster-A in mice reduced dietary lipid absorption in the small intestine and circulation, which suggests that cholesterol trafficking in immune cells influences lipid uptake by enterocytes. This link between immune cell homeostasis and intestinal lipid absorption is a surprising finding considering the intrinsic immune role of T<sub>H</sub>17 cells in maintaining the integrity of the mucosa and preventing pathogens from entering the body.

Potentially harmful substances (antigens) that enter the body are broken down into smaller components. These components are presented by major histocompatibility complex molecules on antigen-presenting cells and recognized by T cell receptors (TCRs) on T cells. High cholesterol levels in the plasma membrane stimulate TCR signaling, which affects T cell proliferation (11). Gao et al. observed that T cell activation increased the amount of accessible cholesterol available in the plasma membrane. However, Aster-A activity swiftly reduced the amount of this cholesterol in the membrane, which mitigated TCR signaling and the activation and expansion of T<sub>H</sub>17 cells. Furthermore, the interaction between Aster-A and stromal interaction molecule 1 (STIM1), a protein that regulates calcium (Ca2+) flux across the plasma membrane, was required for the movement of accessible cholesterol from the plasma membrane to the endoplasmic

128 9 OCTOBER 2025 Science

What is the role of the gut microbiota in this scenario? Gao *et al.* observed that interleukin-22 (IL-22), a cytokine involved in gut homeostasis and mucosal defense (*12*), acts as a signaling molecule between T cells and enterocytes to impair lipid absorption. Segmented filamentous bacteria of the gut microbiota can induce T cells to produce IL-22 (*13*). Gao *et al.* observed that mice treated with broad-spectrum antibiotics to induce dysbiosis had reduced expression of IL-22. Lipid uptake was restored in dysbiotic mice with a T cell-specific Aster-A deficiency.

The study of Gao  $et\ al.$  highlights the importance of the interplay between gut microbes, immune cells, and intestinal epithelial cells in the regulation of dietary fat absorption. The authors have worked out many elements of a complex signaling cascade underlying cell-to-cell communication. Aster-A controls the response of  $T_H17$  cells to gut microbes. Loss of Aster-A in  $T_H17$  cells increases the plasma membrane's accessible free-cholesterol content, enhancing TCR signaling and gut microbe–dependent IL-22 production. These processes then reduce intestinal absorption of dietary lipids in enterocytes and inhibit dietinduced obesity.

How lipid flux into enterocytes is altered by Aster-A in immune cells remains to be determined. It might involve intestinal fatty acid transporters such as CD36 in enterocytes (3), modification of the composition of the enterocyte's apical plasma membrane by lysophosphatidylcholine acyltransferases (4), or the emulsification process in the lumen of the small intestine.

For researchers in the cardiometabolic disease field, the finding that a loss of Aster-A confers resistance to diet-induced obesity, including fatty liver, could be of major interest. The discovery of drugs that target systemic lipid absorption is attracting considerable interest, as dietary lipids accumulate not only in adipocytes and hepatocytes but also in various cancer cells, including those in human colorectal tumors (14). In mice with hypercholesterolemia, excess cholesterol is deposited into the plasma membranes of T cells (15), potentially promoting immunemediated diseases. In this case, the removal of cholesterol from the plasma membrane by Aster-A might have an anti-inflammatory role by dampening inflammatory responses.

It will be intriguing to explore to what extent the interplay between microbes, immune cells, and enterocytes that has been uncovered in mice also governs dietary lipid absorption in humans. Future studies may reveal the physiological importance of this signaling pathway in metabolism and inflammation and open avenues to new therapeutic strategies.  $\square$ 

#### **REFERENCES AND NOTES**

- 1. Y. Gao et al., Science 390, eadt 4169 (2025).
- 2. R. Sender, S. Fuchs, R. Milo, PLOS Biol. 14, e1002533 (2016).
- 3. M. M. Hussain, Curr. Opin. Lipidol. 25, 200 (2014).
- 4. B. Wang et al., Cell Metab. 23, 492 (2016).
- 5. A. Kindt et al., Nat. Commun. 9, 3760 (2018).
- 6. P.D. Cani et al., Nat. Rev. Gastroenterol. Hepatol. 19, 625 (2022).
- 7. L.W. Peterson, D. Artis, *Nat. Rev. Immunol.* **14**, 141 (2014).
- 8. T. Naito et al., eLife 8, e51401 (2019).
- 9. G. van Meer, D. R. Voelker, G. W. Feigenson, Nat. Rev. Mol. Cell Biol. 9, 112 (2008).
- 10. E. Ikonen, X. Zhou, Dev. Cell 56, 1430 (2021).
- 11. W. Yang et al., Nature **531**, 651 (2016).
- 12. M. Keir, Y. Yi, T. Lu, N. Ghilardi, J. Exp. Med. 217, e20192195 (2020).
- 13. I.I. Ivanov et al., Cell **139**, 485 (2009).
- 14. J. Ecker et al., Gastroenterology 161, 910 (2021).
- 15. A. H. Pollock et al., J. Immunol. 196, 3993 (2016).

#### **ACKNOWLEDGMENTS**

J.E. acknowledges support from Deutsche Forschungsgemeinschaft (DFG, German Research Foundation) project nos. 446175916 and 395357507 (SFB 1371, Microbiome Signatures).

10.1126/science.aeb5717

Institute of Clinical Chemistry and Laboratory Medicine, Functional Lipidomics and Metabolism Research, University Hospital Regensburg, Regensburg, Germany. Email: josef.ecker@ukr.de

**MICROBIOLOGY** 

# Natural directed evolution in gut microbiota

Bacteria undergo rapid genetic changes that are selected by alterations in the human gut environment

#### Blair G. Paul<sup>1</sup> and John J. Mekalanos<sup>2</sup>

utation is necessary for evolution, but the prevalent assumption is that most genes maintain a balance between change that supports development of new beneficial attributes and preservation of existing function. Interestingly, two different types of genes emerge when observing genomic variation across large datasets: core, slow-evolving ones, and fast-evolving genes that are presumably responding to environmental changes that lead to rapid adaptation. Microbial cells can tolerate some genetic plasticity but generally have active mechanisms to correct mutations rather than enhance their formation. On page 151 of this issue, Macadangdang et al. (1) describe genomic elements that hypermutate target genes in human gut bacteria. They found that species of the Bacteroides group actively swap these diversitygenerating retroelements (DGRs). Successful recipient bacteria form distinct populations in which specific gene types have been hypermutated by a DGR. The study results strongly suggest that DGRs drive changes selected by perturbations of the gut environment.

DGRs are remarkable elements that diversify their target protein's function through an error-prone mechanism that is mediated by reverse transcriptase, an enzyme that copies RNA into DNA (2). This molecular strategy drives protein diversity because the resulting DNA mutations tend to encode functionally different amino acids rather than the same amino acid or a shorter protein. The variation that DGR hypermutation can theoretically create by rewriting protein-coding DNA sequences is staggering. These elements pack variation into a short region of a target gene where such DNA sequence changes will still encode a viable and functional protein, and a single genome can have up to 14 DGR targets (3). Through their hypermutation, these targets maintain a form of potential evolution that exceeds 10e282 mutant variant combinations. This localized and highly diverse mutagenesis may repeat indefinitely during replication and selection.

Although DGRs were first discovered in bacteriophages (viruses that infect bacteria), they are also common in a diverse range of bacteria and archaea. For example, they are found in archaea from remote seafloor sediments, symbiotic microbes that colonize plant and animal hosts, and nano-sized microbes in groundwater (4-6). However, little was known about DGR biology and its evolutionary importance in the human microbiome.

Bacteria exchange genetic elements with each other in several ways (collectively called horizontal gene trans-

Science 9 OCTOBER 2025 129